

1       **A multi-transcriptomics approach reveals the coordinated action of the**  
2       **endoribonuclease DNE1 and the decapping machinery in orchestrating mRNA**  
3       **decay**

4

5

6       Aude Pouclet<sup>1</sup>, David Pflieger<sup>1</sup>, Rémy Merret<sup>2</sup>, Marie-Christine Carpentier<sup>2</sup>, Marlène  
7       Schiaffini<sup>1</sup>, Hélène Zuber<sup>1</sup>, Dominique Gagliardi<sup>1</sup> and Damien Garcia<sup>1</sup>

8

9       1 Institut de biologie moléculaire des plantes, CNRS, Université de Strasbourg,  
10      Strasbourg, France.

11       2 Laboratoire Génome et Développement des Plantes, Université de Perpignan via  
12      Domitia, CNRS, UMR5096, Perpignan, France.

13

14       **Abstract**

15       Decapping is a crucial step of mRNA degradation in eucaryotes and requires the  
16      formation of the holoenzyme complex between the decapping enzyme DCP2 and the  
17      decapping enhancer DCP1. In Arabidopsis, we recently identified DNE1, a NYN  
18      domain endoribonuclease, as a direct protein partner of DCP1. The function of both  
19      DNE1 and decapping are necessary to maintain phyllotaxis, the regularity of organ  
20      emergence in the apex. In this study we combined *in vivo* mRNA editing, RNA  
21      degradome, transcriptomics and small RNA-omics to identify targets of DNE1 and  
22      study how DNE1 and DCP2 cooperate in controlling mRNA fate. Our data reveal that  
23      DNE1 mainly contacts and cleaves mRNAs in the CDS and has sequence cleavage  
24      preferences. We found that DNE1 targets are also degraded through decapping, and  
25      that both RNA degradation pathways influence the production of mRNA-derived  
26      siRNAs. Finally, we detected mRNA features enriched in DNE1 targets including  
27      RNA G-quadruplexes and translated upstream-ORFs. Combining these four  
28      complementary high-throughput sequencing strategies greatly expands the range of  
29      DNE1 targets and allowed us to build a conceptual framework describing the  
30      influence of DNE1 and decapping on mRNA fate. These data will be crucial to unveil  
31      the specificity of DNE1 action and understand its importance for developmental  
32      patterning.

33

34

35       **Introduction**

36       Eucaryotic cells possess a large panel of general and specific mRNA  
37      degradation activities to precisely set mRNA homeostasis and fine tune gene  
38      expression programs. These activities include: the mRNA decapping complex formed  
39      by the enzyme Decapping 2 (DCP2) and decapping activators including Decapping 1  
40      (DCP1) and Enhancer of decapping 4 (EDC4) (He and Jacobson, 2022; Vidya and  
41      Duchaine, 2022); 5'-3' and 3'-5' exoribonucleases including the exoribonuclease  
42      XRN1 and the RNA exosome complexes (Schmid and Jensen, 2019; Krempl et al.,  
43      2023); several endoribonucleases including ARGONAUTE proteins involved in RNA  
44      silencing (Poulsen et al., 2013), SMG6 involved in nonsense-mediated decay and

45 MARF1 a NYN domain endoribonuclease which acts together with proteins involved  
46 in decapping to regulate the degradation of specific transcripts (Nishimura et al.,  
47 2018; Boehm et al., 2021). DCP2 and exoribonucleases are general factors involved  
48 in bulk mRNA degradation but are also involved in mRNA quality control and  
49 regulatory pathways such as nonsense-mediated decay (NMD) or miRNA-mediated  
50 gene silencing (Rehwinkel et al., 2005; He and Jacobson, 2022). In plants, most of  
51 the activities cited before exist including the decapping enzyme DCP2 in association  
52 with the decapping activators DCP1, VARICOSE (VCS) and EXORIBONUCLEASE 4  
53 (XRN4), the plant homologues of EDC4 and XRN1, respectively, and the plant 3'-5'  
54 RNA exosome (Souret et al., 2004; Zhang et al., 2015; Lange and Gagliardi, 2022). A  
55 specificity of plant is the tight link between RNA degradation and RNA silencing. This  
56 phenomenon is due to the use in plants of a dedicated RNA silencing amplification  
57 machinery to fight against viruses and other invading elements like transposons  
58 (Lopez-Gomollon and Baulcombe, 2022). A key challenge inherent to RNA silencing  
59 amplification is to avoid targeting of its own mRNAs by this defense mechanism. RNA  
60 degradation activities carried by DCP2, XRN4, as well as the RNA exosome, protect  
61 the transcriptome against RNA silencing activation in plants. Indeed, several  
62 mutations in RNA degradation factors lead to the production of mRNA-derived  
63 siRNAs, often resulting in developmental defects (Gregory et al., 2008; De Alba et al.,  
64 2015; Branscheid et al., 2015; Lam et al., 2015; Zhang et al., 2015; Lange et al.,  
65 2019).

66 In the model plant *Arabidopsis thaliana*, we recently identified DNE1 an  
67 endoribonuclease associated with the decapping enhancers DCP1 and VCS and co-  
68 purifying with the RNA helicase UPF1 required for NMD. DNE1 is the closest  
69 homologue of MARF1 and is composed of a NYN endoribonuclease domain  
70 associated with two OST-HTH domains predicted as RNA binding modules. We  
71 found that DNE1 together with decapping are crucial for the precise developmental  
72 patterns appearing during flower emergence in the shoot apex, a phenomenon called  
73 phyllotaxis (Schiaffini et al., 2022). A recent degradome analysis by genome-wide  
74 mapping of uncapped and cleaved transcripts (GMUCT; (Willmann et al., 2014;  
75 Carpentier et al., 2021)) identified 224 mRNAs producing DNE1-dependent RNA  
76 degradation intermediates (Nagarajan et al., 2023). A main achievement of this study  
77 was the identification of the first set of mRNAs targeted by DNE1. Yet, the full  
78 spectrum of DNE1 mRNA targets remains to be discovered, as well as the interplay  
79 between DNE1 and other RNA degradation pathways. In the present study we  
80 combined four complementary high throughput sequencing strategies to identify  
81 mRNAs directly bound and processed by DNE1 and to understand how this  
82 endoribonuclease coordinates its action with the decapping enzyme DCP2 to  
83 orchestrate mRNA decay.

84 First, to identify mRNAs directly in contact with DNE1, we used HyperTRIBE, an *in*  
85 *vivo* RNA editing method in which DNE1 was fused to the catalytic domain of the  
86 adenosine deaminase ADAR (Rahman et al., 2018; Arribas-Hernández et al., 2021).  
87 In order to define which of these mRNAs were processed by DNE1 we applied a  
88 second and complementary approach and analyzed the mRNA degradation patterns

89 influenced by DNE1 using GMUCT. For this approach, we adapted an existing  
90 bioinformatic pipeline for normalization and statistical analysis of GMUCT datasets.  
91 Using this pipeline, we compared GMUCT datasets for *xrn4* and *xrn4 dne1* mutants  
92 and identified more than 1200 loci for which 5' monophosphate mRNA fragments (5'P)  
93 are produced in a DNE1-dependent manner. This result indicates that DNE1 targets  
94 a larger repertoire of mRNAs than previously described. In addition, we also identified  
95 that DNE1 limits the accumulation of decapped RNA degradation intermediates of  
96 some of its targets indicating dual targeting and coordinated action of DNE1 and  
97 decapping. To study this coordinated action of DNE1 and decapping, we analyzed  
98 mutants affected in both DNE1 and DCP2 using transcriptomics and small RNA-  
99 omics approaches. Our results indicate that the cooperation of DNE1 and DCP2  
100 influences the steady state level of several mRNAs and the production of mRNA-  
101 derived siRNAs. Overall, our multi-transcriptomics strategy provides an extended list  
102 of DNE1 targets, identified several mRNA features enriched in DNE1 targets and  
103 identifies nucleotide preferences for DNE1 cleavage. We provide evidences of the  
104 redundancy between the action of DNE1 and decapping in controlling mRNA fate  
105 and in protecting mRNAs against RNA silencing activation. Finally, we propose a  
106 model of the coordinated action of DNE1 and decapping as a conceptual framework,  
107 an important step towards the understanding of how DNE1 and DCP2 cooperate in  
108 the regulation of gene expression and in the control of faithful developmental patterns  
109 in the shoot apex.

110

## 111 **Results**

112

### 113 **Identification of mRNAs associated with DNE1 by mRNA *in vivo* editing**

114 In order to identify mRNAs in direct contact with DNE1, we used the *in vivo* RNA  
115 editing strategy HyperTRIBE (Fig.1; Rahman et al., 2018; Arribas-Hernández et al.,  
116 2021). For this purpose, we generated *Arabidopsis* transgenic lines expressing the  
117 catalytic domain of the adenosine deaminase ADAR from *Drosophila melanogaster*  
118 (hereafter called ADAR) fused to either WT DNE1 or to a DNE1 catalytic mutant  
119 (DNE1<sup>D153N</sup>; Fig. 1A). The rationale for the use of the catalytic mutant DNE1<sup>D153N</sup> was  
120 to improve the efficiency of mRNA target edition by limiting their degradation by  
121 DNE1 and by increasing the dwelling time of DNE1 on its targets. For this experiment  
122 five independent transgenic lines of each construct, considered as five biological  
123 replicates were analyzed by RNA-seq and compared with plants expressing an  
124 unfused version of ADAR, used as a control as previously described (Arribas-  
125 Hernández et al., 2021). This analysis resulted in the identification of 322 and 2268  
126 edited mRNAs by DNE1 and DNE1<sup>D153N</sup> respectively (Fig. 1B, Supplemental Data  
127 Set S1). As expected, most mRNAs (306/322) identified using ADAR-DNE1 were  
128 also present in the ADAR-DNE1<sup>D153N</sup> dataset. The catalytic mutant led to a higher  
129 editing efficiency than the WT, in agreement with our initial hypothesis. Strikingly,  
130 more than 80% of the editions by DNE1 occurred within CDS with both DNE1 and  
131 DNE1<sup>D153N</sup> (86.1% and 83.4% respectively, Fig. 1C). This result suggests that DNE1  
132 interacts mainly with transcripts internally and not at the 5' extremity as could be

133 anticipated from its interaction with decapping activators. This preferential internal  
134 contact with mRNAs can be visualized on selected transcripts (Fig. 1D, Supplemental  
135 Fig. S1). Theoretically, we can envision two alternative scenarios for mRNAs  
136 contacting DNE1, either they are in contact with DNE1 and cleaved, or they are in  
137 contact with DNE1 but not cleaved.

138

### 139 **Analysis of mRNA degradation patterns upon DNE1 inactivation implies a dual 140 targeting by DNE1 and decapping**

141 To discriminate between these two scenarios, and gain further insights on the mode  
142 of action and targets of DNE1, we performed degradome analysis using GMUCT (Fig.  
143 2). Our experimental setup allows the use of efficient methods for normalization and  
144 statistical analysis for target discovery and to quantify all RNA fragments, including  
145 the most abundant and secondary 5'P giving access to the complete DNE1  
146 dependent RNA degradation patterns. Differential RNA degradation patterns were  
147 identified by adapting the DEXseq method, originally developed to analyze  
148 differential splicing patterns (Anders et al., 2012), to analyze GMUCT datasets  
149 obtained from biological triplicates. In this analysis, we considered every 5'P  
150 identified for a given transcript and compared these fragments between two genetic  
151 conditions. The analysis was performed comparing *xrn4* to *xrn4 dne1* in order to work  
152 in backgrounds in which 5'P, including those arising from DNE1 activity as an  
153 endoribonuclease, are stabilized and increase the probability to detect them using  
154 GMUCT. We filtered low covered 5'P by removing positions where the mean RPM of  
155 the 3 biological replicates is lower than 1 RPM in all conditions. After differential  
156 analysis using DEXSeq, we kept positions with a Log2FC $\geq 1$  or Log2FC $\leq 1$  and  
157 adjusted p-value (adjPv)  $< 0.05$ . Using this method, we identified 1475 transcripts with  
158 differential degradome patterns in *dne1 xrn4* (Fig. 2A, 2B, 2C, Supplemental Data  
159 Set S2). The main pattern observed was downregulation of 2631 fragments arising  
160 from 1296 individual loci upon mutation of DNE1 in *xrn4* background. This  
161 observation implies that some loci accumulate several DNE1 dependent fragments.  
162 These fragments are expected to include both direct DNE1 cleavage products and  
163 the most stable mRNA degradation intermediates arising from these fragments. This  
164 result supports the previous conclusion that DNE1 acts as a *bona fide*  
165 endoribonuclease targeting mRNAs, leading to the production of RNA degradation  
166 products with 5'-P extremities (Nagarajan et al., 2023). As previous work identified  
167 224 loci producing DNE1-dependent 5'P RNA degradation intermediates with  
168 GMUCT, our experimental setup and bioanalysis pipeline greatly expand the  
169 spectrum of putative direct DNE1 targets. Examples of these downregulated RNA  
170 fragments can be visualized along the transcripts (Fig. 2B, Supplemental Fig. S2A).  
171 One particularity of our analysis is to identify significantly downregulated 5'P including  
172 both the main RNA degradation intermediate and secondary RNA fragments.  
173 Interestingly, 50% of the loci identified previously (111/224; Nagarajan et al., 2023)  
174 are present in our dataset validating the efficiency of our method to identify DNE1  
175 targets. To have a global view of the position of these DNE1 dependent RNA  
176 degradation patterns, we determined their distribution and compared with the overall

177 accumulation of 5'P. We found that the proportion of downregulated fragments was  
178 increased in CDS and 3'UTR compared to all fragments (Fig. 2D), which supports  
179 cleavage by DNE1 mostly in the CDS but also in 3'UTR.  
180 Somewhat counterintuitively, we also found that 575 transcripts showed increased  
181 5'P when DNE1 is mutated. Interestingly almost 70% of these transcripts (396/575)  
182 were also showing decreased RNA fragments with 5' end at distinct positions on the  
183 transcript (Fig. 2A). Such dual up and down patterns can be visualized along the  
184 transcripts (Fig. 2C, Supplemental Fig. S2B). When we compared the localization of  
185 upregulated versus downregulated 5'P along transcripts, we observed that the  
186 proportion of upregulated 5'P is ten times more important in the 5'UTR than the  
187 downregulated 5'P (Fig. 2D). This difference suggests that upregulated 5'P are more  
188 prone to occur close to the TSS, some of them could represent decapped fragments  
189 or be secondary fragments produced from decapped fragments. To test this  
190 hypothesis, we looked in our GMUCT data for fragments identified as decapped sites  
191 by C-PARE (Nagarajan et al., 2019). Among our 155 100 GMUCT sites, 14 384 were  
192 identified as decapped sites in C-PARE. Most of these sites (14 247) do not change  
193 upon mutation of DNE1, indicating that DNE1 does not globally influence decapping.  
194 Interestingly, 137 of these sites change when DNE1 is mutated with a predominance  
195 of upregulated (124) versus downregulated (13) sites. Therefore, mutation in DNE1  
196 can lead to an increased accumulation of decapping intermediates. Upregulated 5'P  
197 occur mainly (70%) on transcripts showing downregulated 5'P at other location,  
198 indicating the dual targeting by DNE1 and decapping. This trend can be visualized on  
199 many loci including AT5G11580, AT3G20898 and AT3G16150 for example (Fig. 2C,  
200 Supplemental Fig. S2B). As we analyzed the complete RNA degradation patterns  
201 including main and secondary sites, some upregulated 5'P likely represent secondary  
202 5'P arising from degradation of decapped intermediates. Such examples can be  
203 visualized on transcripts presenting many 5'P like AT1G22190 for example  
204 (Supplemental Fig. S2B). The RNA degradation patterns with 5'P accumulating more  
205 in *xrn4 dne1* generally occur upstream of decreased 5'P fitting the idea that  
206 upregulated fragments derive from decapped mRNAs and downregulated fragments  
207 derived from DNE1 endoribonucleolytic cleavage either in CDS or 3'UTR. In  
208 conclusion, our experimental setup and exhaustive analysis of DNE1-dependent  
209 RNA degradation patterns greatly expand the spectrum of putative DNE1 targets and  
210 highlights the coordination of the action of DNE1 and decapping.  
211

## 212 **Biased nucleotide composition at DNE1 cleavage sites suggests sequence 213 cleavage preferences**

214 To investigate a potential sequence cleavage preference for DNE1, we analyzed the  
215 nucleotide composition in the vicinity of the main DNE1 dependent fragments. A  
216 nucleotide logo was produced 25 nt before and after the 5' extremity of these  
217 fragments on the 1296 loci with downregulated 5'P in GMUCT. Interestingly, whereas  
218 no bias is observed in a control analysis performed on DNE1-independent 5'P, a  
219 significant deviation from a random nucleotide composition appears in the close  
220 vicinity of these 1296 cleavage sites. The nucleotide bias observed for

221 downregulated 5'P clearly appears both before and after the 5'P extremity at  
222 positions -3 to -6 and -1 to 1 (Fig. 2E). The most extreme values appear at  
223 nucleotides -4, -3 and 0 with 46.7, 44.2 % and 38.6% of G respectively, a strong  
224 deviation from the 25.4% of G observed when considering the whole region. This  
225 non-random sequence composition strongly suggests a sequence preference for  
226 DNE1 cleavage activity.

227

## 228 **Analysis of HyperTRIBE and GMUCT data identifies mRNA features enriched in 229 DNE1 targets**

230 We then compared the data obtained by HyperTRIBE with data obtained by GMUCT  
231 (Fig. 3). We found that *ca* 22% of the transcripts identified as DNE1 targets by  
232 GMUCT (those producing less 5'P fragments in *xrn4 dne1*) were edited by DNE1-  
233 D153N (288/1296) identifying them as in direct contact and processed by DNE1 (Fig.  
234 3A). We investigated the presence of specific features in mRNAs identified in these  
235 two approaches. Because G-rich motifs were previously identified in DNE1 targets  
236 (Nagarajan et al., 2023) and because the first OST-HTH domain of DNE1 was found  
237 to interact with G-rich and RNA G-quadruplex structures (rG4) in vitro (Ding et al.,  
238 2020), we first looked for the overlap between HyperTRIBE and experimentally  
239 validated loci containing rG4 (Yang et al., 2020); Fig. 3B). Interestingly we found that  
240 516 mRNAs directly in contact with DNE1 in HyperTRIBE were containing  
241 experimentally validated rG4 in rG4-seq. To determine if DNE1 targets identified by  
242 HyperTRIBE and GMUCT were enriched for specific features, we looked at the  
243 distribution of diverse mRNA features among these loci, including CDS, UTR length  
244 and intron number (Fig. 3C). Whereas no consistent changes were observed  
245 between the different lists for CDS and intron numbers, DNE1 targets identified by  
246 these methods seemed to systematically harbor slightly longer UTRs. Because of  
247 these longer UTRs and the presence of mRNA with rG4 among DNE1 targets, we  
248 tested whether the proportion of transcripts containing translated uORFs in 5'UTR  
249 (Ribo-seq data from (Hu et al., 2016)) or validated rG4 (rG4-seq data from (Yang et  
250 al., 2020)) was higher among DNE1 targets compared to all transcripts expressed in  
251 similar tissues either seedlings or flowers. Interestingly, we observed a significantly  
252 higher proportion of mRNA containing translated uORFs and rG4 among identified  
253 DNE1 targets (Fig. 3D). Strikingly, for both the strongest enrichments were observed  
254 for DNE1 targets identified in common between GMUCT and HyperTRIBE,  
255 reinforcing the relevance of these features (Fig. 3C, 3D, Supplemental Data Set S6  
256 and S7). Overall, this comparison identifies a set of 288 transcripts directly in contact  
257 and processed by DNE1 and reveals that these targets of DNE1 validated by two  
258 independent techniques, are enriched in rG4 and translated uORFs.

259

## 260 **Mutations in *DNE1* and *DCP2* lead to synergistic transcriptomic changes**

261 To better understand the impact and coordinated action of DNE1 and decapping on  
262 the transcriptome, we performed a transcriptomic analysis on a series of mutants  
263 including *dcp2* (*its1*, a previously described hypomorphic allele of *dcp2*), *dne1*, *dne1*  
264 *dcp2* and *xrn4* (Fig. 4). Our working hypothesis from previous work and phenotypic

265 analysis of these mutants predicts that combining mutations in *DNE1* and *DCP2*  
266 should synergistically affect the transcriptome and that *xrn4* and *dne1 dcp2* might  
267 affect some similar transcripts. Accordingly, we observed that whereas *dne1* and the  
268 weak allele of *dcp2* have a modest impact on the transcriptome (Fig. 4A), this effect  
269 is exacerbated in the two *dne1 dcp2* double mutant combinations (*dne1-2 dcp2* and  
270 *dne1-3 dcp2*, Fig. 4A, Supplemental Data Set S3). Overall, the most prominent trend  
271 observed in *dne1 dcp2* is upregulated transcripts and illustrate the synergistic effect  
272 of combining *dne1* and *dcp2* on the steady state level of specific mRNAs. Comparing  
273 these upregulated transcripts in *xrn4* and *dne1 dcp2*, two genetic backgrounds  
274 showing similar developmental defects, revealed that 51 transcripts were commonly  
275 deregulated in these mutants (Fig. 4B, 4C). These genes represent good candidates  
276 to identify genes involved in the phyllotactic defects observed. They notably include  
277 three bHLH transcription factors, PERICYCLE FACTOR TYPE-B 1 (PFB1:  
278 AT4G02590), LONESOME HIGHWAY LIKE 1 and 2 (LHL1: AT1G06150 and LHL2:  
279 AT2G31280). PFB1 is known to govern the competence of pericycle cells to initiate  
280 lateral root primordium, its involvement in organ emergence in the shoot is currently  
281 unknown (Zhang et al., 2021). LHL1 and LHL2 are known to regulate early xylem  
282 development downstream of auxin in roots and interestingly the use of an online tool  
283 to predict expression in the shoot apex indicate that both genes are expressed  
284 around the shoot apical meristem (Zhang et al., 2021); Supplemental Fig. S3). A  
285 fourth gene RAP2.4 for RELATED TO AP2 4 (AT1G78080) caught our attention.  
286 RAP2.4 it is an ethylene responsive factor, interestingly ERF12 another AP2 ethylene  
287 response factor was recently shown to be required for phyllotaxis (Chandler and Werr,  
288 2020). These genes represent good candidates to better understand the importance  
289 of *DNE1*, *DCP2* and *XRN4* in phyllotaxis formation. Focusing on genes commonly  
290 upregulated in the two *dne1 dcp2* double mutants we asked whether some of them  
291 were identified as direct targets of *DNE1* in either GMUCT or HyperTRIBE. We found  
292 that among these 68 genes 7 are found in GMUCT and 20 are found in HyperTRIBE  
293 for a total of 21 genes identified as putative direct targets of *DNE1* including RAP2.4  
294 identified in both approaches (Fig. 4D). This result highlights the redundancy of  
295 *DNE1* and *DCP2* in the regulation of gene expression and provides candidate genes  
296 to investigate the importance of these factors for phyllotaxis.

297

## 298 **Differential sRNA populations can be instructive to identify targets of mRNA 299 decay factors**

300 Mutations in mRNA decay factors including *xrn4*, *dcp2* or *ski2* lead to the  
301 accumulation of 21 to 22 nt mRNA-derived siRNAs (Gregory et al., 2008; De Alba et  
302 al., 2015; Branscheid et al., 2015; Zhang et al., 2015). This phenomenon is due to  
303 the conversion of stabilized mRNA decay intermediates into siRNAs by the action of  
304 the RNA silencing machinery. Interestingly, several of these mRNA-derived siRNAs  
305 affect plant development as observed in *dcp2*, *xrn4* *ski2*, *urt1* *xrn4* (De Alba et al.,  
306 2015; Zhang et al., 2015; Scheer et al., 2021). Studying these siRNA populations  
307 have thus a double interest, it could help the identification of siRNAs potentially  
308 involved in the developmental defects appearing in corresponding mutants and it

309 could allow the identification of mRNA targets of DNE1 and DCP2. To determine if  
310 the production of mRNA-derived siRNAs in RNA degradation mutants can be used as  
311 a criterion to identify targets of mRNA decay factors, we first analyzed small RNA  
312 populations accumulating in *xrn4* and *dcp2* (Fig. 5). XRN4 and DCP2 act sequentially  
313 in mRNA decay, the prediction is that they should accumulate populations of mRNA-  
314 derived siRNAs on similar loci. As expected, the main trend observed in *xrn4* and  
315 *dcp2* was upregulated mRNA-derived siRNAs populations (4737 loci in *xrn4*, and  
316 2386 loci in *dcp2*, Fig. 5A, Supplemental Data Set S4). Interestingly, we observed a  
317 major overlap between siRNA loci in both mutants (with 2186 common loci, Fig. 5B).  
318 Of note, some of these loci are known *bona fide* targets of XRN4 including some of  
319 the first validated XRN4 targets, AT4G32020 and AT1G78080 (Souret et al., 2004).  
320 This first comparison shows that we can use mRNA-derived siRNA signatures  
321 differentially accumulating in RNA decay mutants to identify targets of mRNAs decay  
322 factors.

323

### 324 **Small RNA sequencing identifies DNE1-dependent small RNA populations**

325 We used the same approach to identify mRNAs targeted by DNE1 by looking at  
326 mRNA-derived siRNA signatures differentially accumulating upon mutation of DNE1.  
327 In this analysis, we analyzed *dne1-2*, *dne1-3* and the corresponding *dne1 dcp2*  
328 double mutants. Globally, we found little changes in mRNA-derived siRNA  
329 accumulation in single *dne1* mutants and more changes in *dne1 dcp2* (Fig. 5A). This  
330 increase in the double mutant is largely due to the *dcp2* mutation as we observed a  
331 large overlap between sRNA populations upregulated in *xrn4*, *dcp2* and *dne1 dcp2*  
332 (Fig. 5B, 1460 loci).

333 This first analysis did not reveal a significant impact of mutation in DNE1 on siRNA  
334 accumulation. To investigate this point further we performed a differential analysis of  
335 siRNAs in *dne1 dcp2* using *dcp2* as a reference. In this analysis we identified two  
336 opposite trends, upregulated siRNA populations (69 loci in *dne1-2 dcp2* and 67 loci in  
337 *dne1-3 dcp2*, Fig. 5C) and downregulated siRNA populations (123 loci in *dne1-2*  
338 *dcp2* and 126 loci in *dne1-3 dcp2*, Fig. 5C). An important overlap was observed  
339 between the two double mutants with 52 loci for upregulated siRNAs and 97 loci for  
340 downregulated siRNAs in common in both *dne1 dcp2* combinations (Fig. 5D). Both  
341 tendencies could be validated on a siRNA northern blot, which also illustrates that  
342 many of these siRNA species are produced in an *xrn4* mutant (Fig. 5E). Of note we  
343 analyzed in these blots triple *xrn4 dcl2 dcl4* mutants, which confirmed that these  
344 siRNAs are produced by the RNA silencing machinery and involve the two main  
345 Dicer-like proteins involved in RNA silencing amplification DCL4 and DCL2. To better  
346 describe these patterns, we inspected the distribution of these siRNA on the  
347 transcripts. We observed that the siRNA distribution is different between upregulated  
348 and downregulated siRNAs. Upregulated siRNAs are mainly located on the CDS and  
349 3'UTR (40/52, Fig. 5F Up, Supplemental Fig. S4A, Supplemental Data Set S5), in  
350 contrast downregulated sRNAs were mainly arising from 5'UTR (65/97; Fig. 5F Down,  
351 Supplemental Fig. S4 Down, Supplemental Dataset S5). We looked at the distribution  
352 of diverse mRNA features, including CDS, UTR length and intron number, in the loci

353 associated with each trend compared to overall expressed genes (Fig. 5G). The most  
354 striking feature for loci with upregulated siRNAs was a strikingly low intron number,  
355 identifying those loci as intron-poor mRNAs. In contrast loci with less siRNAs  
356 possess the same number of introns than other expressed transcripts and had  
357 slightly longer 3'UTR and strikingly longer 5'UTR. We then tested whether loci with  
358 differential siRNA patterns were particularly enriched in transcripts containing  
359 translated uORFs in 5'UTR or rG4, as observed in mRNA identified as DNE1 targets  
360 in GMUCT and HyperTRIBE. The most striking result of this analysis appeared for  
361 loci with downregulated siRNAs in *dne1 dcp2* versus *dcp2* (already identified to  
362 harbor dramatically longer 5'UTR), which were noticeably enriched in mRNA  
363 containing translated uORFs (Fig. 5H). In terms of siRNA accumulation, the general  
364 trend for upregulated and downregulated siRNAs is the exacerbation or attenuation  
365 of siRNA populations observed in *dcp2* (Fig. 5F), suggesting that both DCP2 and  
366 DNE1 target those transcripts. Despite the relatively low number of differential loci  
367 found in siRNA-seq we found an overlap between loci found in siRNA sequencing,  
368 HyperTRIBE and GMUCT (Fig. 6). Overall, 44 loci showing differential siRNA  
369 patterns were identified as DNE1 targets by GMUCT or HyperTRIBE suggesting that  
370 they represent *bona fide* DNE1 targets. One of the most striking examples of this  
371 trend is the RAP2.4 gene AT1G78080, which was recovered in every HTS methods,  
372 it is heavily edited by DNE1-D153N mainly in the CDS (Supplemental Fig. S1), it  
373 presents both upregulated and downregulated RNA fragments in *dne1 xrn4* in  
374 GMUCT (Supplemental Fig. S2B), its mRNA is upregulated in *dne1 dcp2* in RNA-seq  
375 (Fig. 4C) and it produces less siRNA in *dne1 dcp2* versus *dcp2* in its 5'UTR  
376 (Supplemental Fig. S4B). These observations indicate that every method used in this  
377 study, despite the fact that they monitor completely different features, has the  
378 potential to identify DNE1 targets highlighting the added value of our multi-  
379 transcriptomic approach.

380

## 381 **Discussion**

382  
383 In this work we combined *in vivo* RNA editing by HyperTRIBE and RNA degradome  
384 sequencing by GMUCT to identify targets of the endoribonuclease DNE1. The  
385 advantage of HyperTRIBE is to identify mRNAs contacting DNE1 but its intrinsic  
386 limitation is that it does not give any indication regarding mRNA cleavage by DNE1.  
387 The advantage of using GMUCT is to identify mRNAs cleaved by DNE1 but its  
388 limitation is that this identification is only possible if the corresponding RNA  
389 degradation products are sufficiently stable. These limitations are solved when  
390 combining HyperTRIBE with GMUCT giving access to independent lists of targets. In  
391 addition, the overlap between the two methods identifies a refined list of mRNAs  
392 contacting and cleaved by DNE1.

393 In our work we also interrogated the influence of DNE1 and DCP2 on mRNA fate  
394 using transcriptomics and small RNA deep sequencing in the *dne1 dcp2* double  
395 mutant. While transcriptomics identified mRNAs with altered steady state levels in  
396 *dne1 dcp2*, the most interesting information regarding DNE1 action and coordination

397 with DCP2 came from the study of mRNA-derived siRNAs. The identification of  
398 differential mRNA-derived siRNAs in *dne1 dcp2* compared to *dcp2* supported the  
399 hypothesis of their action on similar transcripts. We consider changes in mRNA-  
400 derived siRNA production in *dne1 dcp2* as a readout of changes in mRNA fate when  
401 DNE1 function is abrogated. Unexpectedly, two trends appeared in this analysis,  
402 upregulated siRNAs and downregulated siRNAs. We propose a model to explain the  
403 appearance of these two opposite trends. Our interpretation of this result is that both  
404 trends appear on mRNAs targeted by DNE1. This is coherent with the presence of  
405 some of these loci in GMUCT and/or HyperTRIBE. Upregulated siRNAs are  
406 produced all along the transcripts in *dcp2*, suggesting that they are produced from  
407 full-length mRNAs that are stabilized when DCP2 function is affected. In *dcp2*, DNE1  
408 cleaves a pool of these transcripts reducing the pool of full-length transcripts  
409 available for decapping. When DNE1 is mutated the pool of full-length transcripts  
410 increases leading to increased targeting by DCP2. This increased targeting by DCP2  
411 leads in *dne1 dcp2* to increased proportion of stabilized full-length mRNAs and  
412 increased siRNA accumulation, likely produced from full-length capped mRNAs (Fig.  
413 7, panel A).

414 In contrast downregulated siRNAs are mainly produced in discrete positions from  
415 5'UTRs. Our interpretation is that they are not produced from full-length mRNA but  
416 from stabilized DNE1 cleavage products. In this case abrogating DNE1 action in  
417 *dne1 dcp2* leads to the reduction in the accumulation of DNE1 cleavage products  
418 and a reduction in mRNA-derived siRNA production from these products (Fig. 7B).  
419 This interpretation implies that DNE1 cleavage products can be decapped by DCP2.  
420 In addition of this mechanistic model, we found that these two lists of mRNAs are  
421 enriched for very different features. mRNAs with upregulated siRNAs are strikingly  
422 intron-poor mRNAs. This is reminiscent of previous studies on transgenes, in which it  
423 was described that introns protect transgenes from RNA silencing activation (Christie  
424 et al., 2011). We propose that these mRNAs are specifically prone to siRNA  
425 production due to their low introns number, this low intron number trend was also  
426 identified but to a slightly lower extent for mRNAs producing siRNAs in *xrn4* and *dcp2*  
427 in our data (Fig. 5G). This results strongly support the hypothesis that in RNA  
428 degradation mutants, introns protect mRNAs from RNA silencing activation as  
429 previously observed in WT plants (Christie et al., 2011). In contrast mRNAs with  
430 downregulated siRNAs had similar intron numbers as overall expressed mRNAs but  
431 were characterized by strikingly longer 5'UTR. Interestingly, we found that these long  
432 5'UTR were significantly enriched in translated uORFs, coinciding with the sites of  
433 siRNA production in *dcp2*. We can speculate that the translation of these uORFs  
434 might further stabilize these cleavage products allowing them to partially escape 3' to  
435 5' degradation leaving enough time for them to be detected and processed by the  
436 RNA silencing machinery leading to siRNA production.

437 How DNE1 recognizes its targets and what is the trigger to induce DNE1 mediated  
438 RNA degradation are fundamental questions to be addressed in future studies.  
439 Definitive answers to these questions will require more work but the identification of  
440 enriched features among DNE1 targets can be instructive to formulate hypothesis.

441 First, we identified that transcripts identified in the HyperTRIBE and GMUCT  
442 approaches are enriched in translated uORFs and rG4. Remarkably, this trend is  
443 exacerbated in the highest confidence DNE1 targets commonly identified in GMUCT  
444 and HyperTRIBE (Fig. 3C). This observation suggests that translated uORFs and  
445 rG4 might promote targeting and cleavage by DNE1. Of note, for many transcripts  
446 identified to contact DNE1 in HyperTRIBE, we did not detect differential RNA  
447 fragments in GMUCT. A possible explanation for this discrepancy is that DNE1 might  
448 contact both targets and non-targets in a scanning mode, looking for cleavage  
449 inducing features. Hallmarks of this potential scanning can be found in the  
450 HyperTRIBE results (Supplemental Fig. S1) as some targets were edited all along  
451 the CDS. Translated uORFs are known to regulate gene expression by impairing  
452 translation of the main ORF. In this scenario, DNE1 would scan mRNAs containing  
453 translated uORF with inefficient translation of the main ORF. The inefficient  
454 translation of the main ORF could allow the formation of tertiary structures in the  
455 main ORF including rG4. While DNE1 scans these mRNAs it encounters rG4 or other  
456 structures, they are recognized by the OST-HTH domains of DNE1, identified as G  
457 rich and rG4 interacting domains *in vitro* and induce cleavage by DNE1. Our analysis  
458 of DNE1 cleavage sites revealed a biased nucleotide composition. The identification  
459 of this nucleotide preference at DNE1 cleavage site is fundamentally different from  
460 the previous identification of an enriched G-rich motif (YGGWG) in the vicinity of  
461 DNE1 cleavage site (Nagarajan et al., 2023). While the YGGWG motifs are found at  
462 various positions surrounding the cleavage site, the nucleotide preference identified  
463 here occurs at very precise position on and around cleavage sites. Interestingly, a  
464 similar nucleotide preference appeared when we performed the logo analysis on the  
465 224 DNE1 targets identified in the previous study (Supplemental Fig. S2C), validating  
466 the efficiency of our identification of 1295 DNE1 target in GMUCT and the relevance  
467 of this logo. This observation reveals that DNE1 does not cleave mRNAs at random  
468 sequences and support the hypothesis that DNE1 have nucleotide context  
469 preferences for its endonuclease activity. To sum up the previous observations we  
470 build a final model illustrating the coordinated action of DNE1 and DCP2 in the  
471 degradation of DNE1 targets (Fig 7C).

472 Overall, our study greatly increases the spectrum of potential DNE1 targets. It will be  
473 crucial to pursue the efforts and to start investigating how DNE1 regulates specific  
474 processes at the tissues level. We previously showed that together with DCP2, DNE1  
475 is required for phyllotaxis, the formation of precise developmental patterns at the  
476 shoot apex. Our current work provides a first extended list of DNE1 targets that can  
477 be searched to identify novel regulators of phyllotaxis. Which of these targets are  
478 locally expressed in developing primordia? How their expression is altered upon  
479 mutation in DNE1 and DCP2 and what are the physiological changes in the shoot  
480 apex in *dne1 dcp2*? Answers to these questions will be crucial to better understand  
481 the importance of these factors for phyllotaxis and combining the study of *dne1 dcp2*  
482 and *xrn4* will reveal the overall importance of RNA degradation in the control of the  
483 homeostasis of key regulators of phyllotaxis.

484

485 **Materials and methods**

486

487 **Plant materials and growth conditions**

488 *Arabidopsis thaliana* mutants and WT lines were in the Columbia-0 (Col-0) ecotype.  
489 Mutants used in this study were all previously described: *dne1-1* (Salk\_132521);  
490 *xrn4-3* (SALK\_014209); *dcl2-1* (SALK\_064627), *dcl4-2* (GABI\_160G05), *dne1-2* and  
491 *dne1-3* were produced by the CRISPR/Cas9 system (Schiaffini et al., 2022).  
492 Transgenic lines produced in the HyperTRIBE strategy were in the *dne1-3* mutant  
493 background. The plant material used for RNA-seq, small RNA-seq and HyperTRIBE  
494 were grown on soil in 16/8h light/dark conditions until flowering and unopened flower  
495 buds were collected. The plant material used for GMUCT were seedlings grown on  
496 Murashige and Skoog (MS) medium (MS0255 Duchefa, 0,7% w/v agar, pH 5.7).  
497 Seeds were sterilized with bleach/ethanol solution (0,48% / 70%) on shaker for 10min,  
498 and then wash with 70% ethanol. The seed were rinse twice with sterile water. After  
499 24h of stratification at 4°C seedlings were grown in 16/8 h light/dark conditions at  
500 21°C for 10-d and transferred into liquid half-strength MS medium. The seedlings  
501 were collected for RNA extraction after incubation at 40 rpm under constant light for  
502 24h.

503 **Constructs produced for HyperTRIBE**

504 p35S:FLAG-ADARcd<sup>E488Q</sup>-DNE1-35ST (F-ADAR-DNE1), p35S:FLAG-ADARcd<sup>E488Q</sup>-  
505 DNE1<sup>D153N</sup>-35ST (F-ADAR-DNE1<sup>D153N</sup>), ADARcd<sup>E488Q</sup> (p35S:FLAG-ADARcd<sup>E488Q</sup>-  
506 35ST (FLAG-ADAR). Constructs were produced by overlap-extension PCR (Bryksin  
507 and Matsumura, 2013) to fuse the ADAR sequence to DNE1 followed by Gateway®  
508 recombination in pH2GW7. All final constructs were verified by Sanger sequencing  
509 and mobilized into *Agrobacterium tumefaciens* (GV3101 pMP90) chemically  
510 competent cells. Transgenic lines were generated by floral dip (Clough and Bent,  
511 1998) of *dne1-3* with *A. tumefaciens* GV3101 bearing pH2GW7 F-ADAR-DNE1, F-  
512 ADAR-DNE1<sup>D153N</sup> and FLAG-ADAR. Selection of primary transformants (T1) was  
513 done by hygromycin to select five independent lines for each type of transgene.  
514 Expression levels were assessed by western blot using anti-FLAG M2 antibodies.  
515 (Primers used in the study present supplemental table S1)

516

517 **Total RNA extraction**

518 Total RNA was extracted using Tri-Reagent (Molecular Research Center, Inc.,  
519 Cincinnati, OH, USA) according to the manufacturer's instructions, followed by acidic  
520 phenol chloroform extraction and RNA precipitation with ethanol. The samples were  
521 then treated with DNase I (Thermo Fisher Scientific) according to the manufacturer's  
522 instructions.

523

524 **RNA degradome library preparation**

525 Poly(A)+ RNA isolated from 11 days old whole seedlings were used to generate  
526 GMUCT libraries according to the published protocol (Carpentier et al., 2021).  
527 Libraries were sequenced on Illumina HiSeq 2500 in a 50 nt single-end mode.

528

## 529 **Computational analysis of RNA degradome data**

530 GMUCT libraries were aligned to TAIR10 genome with hisat2. The coverage of 5' reads position (for both strands) were extracted using bedtools genomecov from the bam files. A differential expression analysis was performed between *xrn4* and *xrn4* *dne1* (3 replicates per sample) using the DEXSeq R package with the following design: ~ sample + base + condition:base. All the scripts are available at

535 [https://github.com/ibmp/dne1\\_2024](https://github.com/ibmp/dne1_2024).

536

## 537 **HyperTRIBE library preparation**

538 The HyperTRIBE analysis was performed on five independent lines of F-  
539 ADARcd<sup>E488Q</sup> (control), F-ADARcd<sup>E488Q</sup>-DNE1 and F-ADARcd<sup>E488Q</sup>-DNE1<sup>D153N</sup> used  
540 as five biological replicates. Purified total RNAs were quantified by Qubit (Invitrogen)  
541 fluorimeter, quality was assessed using Bioanalyzer 2100 (Agilent) system. Six  
542 hundred nanograms of RNAs were used for library preparation with the TruSeq®  
543 Stranded mRNA Library Prep following manufacturer's instructions. Libraries were  
544 sequenced by paired-End (2x100bases) on an Illumina HiSeq 4000. Sequencing was  
545 performed by the GenomEast platform.

546

## 547 **Computational analysis of HyperTRIBE**

548 Sequencing data were aligned to the TAIR10 reference genome with hisat2 using the  
549 following options: "-t -k 50 --max-intronlen 2000 --rna-strandness RF --no-unal". The  
550 analysis was conducted following the steps described here <https://github.com/sarah-ku/hyperTRIBER>. In short, the bam files were split by strand and a single mpileup file  
551 was generated from all the files with samtools. The mpileup file was then converted  
552 using the RNAeditR\_mpileup2bases.pl script. The resulting output was further  
553 analyzed in R with the hyperTRIBER package. Only A-to-G edits were selected.

555

## 556 **RNAseq library preparation**

557 The RNAseq analysis was performed on biological triplicates of inflorescence of the  
558 WT, *its1* (*dcp2*), *dne1-2*, *dne1-3*, *xrn4-3* and two double mutant *its1 dne1-2* and *its1*  
559 *dne1-3*. Purified total RNAs were quantified by Qubit (Invitrogen), RNA quality was  
560 tested using Bioanalyzer 2100 (Agilent) system. Six hundred nanograms of RNAs  
561 were used for library preparation with the TruSeq® Stranded mRNA Library Prep  
562 using manufacturer's instructions. Libraries were sequenced by single read  
563 (1x50bases) with an Illumina HiSeq 4000. Sequencing was performed by the  
564 GenomEast platform.

565

## 566 **Computational analysis of RNAseq**

567 Reads were first aligned to the TAIR10 reference genome using hisat2 aligner with  
568 the following options:

569 --max-intronlen 2000 -q --rna-strandness R --passthrough --read-lengths 50

570 Then, read counts were extracted for each representative transcript using  
571 FeatureCounts and a differential expression analysis was performed in R with the

572 DESeq2 package. For all analyses, we used the most representative gene isoform  
573 (described in the TAIR10\_representative\_gene\_models file).

574

### 575 **sRNAseq library preparation**

576 Transcriptomic analysis was performed on biological triplicates of inflorescence of the  
577 wild type (col-0), *its1* (*dcp2*), *dne1-2*, *dne1-3*, *xrn4-3* and two double mutant *its1*  
578 *dne1-2* and *its1 dne1-3*. Purified total RNAs were quantified by Qubit (Invitrogen)  
579 fluorimeter, RNA's quality was tested using Bioanalyzer 2100 (Agilent) system. Six  
580 hundred nanograms of RNAs were used for libraries preparation with the NEBNext®  
581 Multiplex Small RNA Library Prep Set for Illumina® using manufacturer's instructions.  
582 Libraries were sequenced by single read (1x50bases) with an Illumina HiSeq 4000.  
583 Sequencing was performed by the GenomEast platform.

584

### 585 **Computational analysis of sRNAseq**

586 Raw reads were trimmed using trimgalore with the following options: “-q 30 --max\_n  
587 5 --max\_length 30”. The resulting clean reads were mapped to TAIR10 reference  
588 genome with the following options: “-v 1 --best --strata -k 10”. The sRNA counts per  
589 size on each TAIR10 representative transcripts were extracted from each bamfile  
590 with ShortStack using the following options: “--nohp --dicermin 15 --dicermax 30”. To  
591 study mRNA-derived siRNAs, a differential expression analysis was done with  
592 DESeq2 using as counts the sum of 21 and 22nt long sRNAs in each transcript  
593 features. Extraction of DicerCall 21-dependent transcripts: the bam files from all  
594 replicates (3 replicates per sample) were merged into a single bam per sample.  
595 ShortStack was run on each merged bam. Loci identified as “DicerCall21” by  
596 ShortStack were extracted from the results. Subsequently, we selected loci that were  
597 found in at least 3 conditions out of 7 as DicerCall 21-dependent transcripts, resulting  
598 in a list of 7935 AGI.

599

### 600 **Low molecular weight northern blot**

601 For this analysis we used 40ug of total RNA resuspended in sRNA loading buffer (4X:  
602 50% glycerol, 50mM Tris pH 7.7, 5mM EDTA, 0.03% bromophenol Blue). The RNA  
603 was denatured at 95°C for 5min prior to loading in a prewarmed 17.5%  
604 acrylamide:bis 19:1; 7M urea, 0.5X TBE gel, electrophoresis was performed in 0.5  
605 TBE at 80V for 5h. RNA was transferred onto an Amersham Hybond-NX membrane  
606 at 300mA in 0.5x TBE for 1h at 4°C. The membrane was chemically crosslinked with  
607 EDC (1-ethyl-3-(3-dimethylaminopropyl) carbodiimide) for 1h30 at 60°C. After  
608 crosslinking, the membrane was rinsed with water and incubated at 42°C for 45min in  
609 PerfectHyb™ plus hybridization buffer. For probes produced by random priming, the  
610 purified PCR products were radiolabeled using the Prime-a-Gene® Labeling System  
611 according to the manufacturer's instructions. For probes produced by end labeling,  
612 the primers were radiolabeled using the Thermo Scientific™ T4 Polynucleotide  
613 Kinase according to the manufacturer's instructions. Radiolabelled probes were  
614 added directly in the buffer and the membrane was incubated overnight (O/N) with  
615 the probe at 42°C. The membrane was washed with 2xSSC (0.3M NaCl, 30mM

616 sodium citrate) 2% SDS three times 20 min at 50°C. Signal intensities were analyzed  
617 using the Typhoon system (GE Health Sciences). Membranes were stripped in  
618 boiling 0.1% SDS three times 20min. Northern blot results presented are  
619 representative of 3 biological replicates. Primers used for probe preparation are listed  
620 in supplemental table S1.

621

## 622 **Protein extraction and Western blotting.**

623 Total protein was extracted using Tri-Reagent (MRC). Five flower buds were ground  
624 in 300  $\mu$ l TRI-Reagent. After mixing 60  $\mu$ l of chloroform were added then the sample  
625 is incubated 15 min at room temperature then centrifugated 15 min. After removing  
626 the aqueous phase, DNA is precipitated by adding 100 $\mu$ l ethanol, incubating for  
627 15min and centrifuging for 15min at 18,000g. The supernatant was then recovered,  
628 and the proteins were precipitated by adding 3V of 100% acetone, followed by 5min  
629 incubation on ice. After centrifugation 1min at 5000g, the pellet was washed once  
630 with 80% acetone. The pellet was then recovered in SDS-urea buffer. (62.5 mM Tris  
631 pH 6.8, 4 M urea, 3% SDS, 10% glycerol, 0.01% bromophenol blue). The samples  
632 were separated by SDS-PAGE and transferred to a 0.45  $\mu$ m Immobilon-P PVDF  
633 membrane (Millipore). The membrane was incubated 2h at 4°C with ANTI-FLAG  
634 antibodies® M2-peroxydase (Sigma-Aldrich, used at 1/ 1000 dilution). The antibodies  
635 were detected by using Lumi-Light Western Blotting Substrate (Roche). Pictures  
636 were taken with a Fusion FX camera system (Vilber). The PVDF membranes were  
637 stained with 0.1% Coomassie Brilliant Blue R-250, 9% acetic acid, 45.5% ethanol) to  
638 monitor loading.

639

## 640 **Comparison of HTS datasets with transcript characteristics**

641 The number of introns and the length of CDS and UTRs used for the comparison  
642 were based on the TAIR10 annotation for representative transcripts. The proportion  
643 of mRNA containing uORFs and rG4 were retrieved from Hu et al. 2016 and Yang et  
644 al. 2020, respectively. For the control lists, we used the lists of transcripts detected by  
645 RNAseq in WT flowers (this paper, Supplemental Data Set S3) and in WT seedlings  
646 (Schiaffini et al. 2022). Boxplots shown Fig.3 and 5 displays the median, first and  
647 third quartiles (lower and upper hinges), the largest value within 1.5 times the  
648 interquartile range above the upper hinge (upper whisker) and the smallest value  
649 within 1.5 times the interquartile range below the lower hinge (lower whiskers). In  
650 Fig.3C and 4C, statistical analysis was performed using Pairwise Wilcoxon Rank  
651 Sum Tests with data considered as unpaired (non-parametric test, two-tailed). In  
652 Fig.3D and 4D, a two-samples z-test of proportions was applied. For all statistical  
653 analysis, an adjusted p-value (fdr) of 0.001 was defined as threshold of significance.  
654 Plots and statistics were performed using R (v4.2.2), and R packages ggplot2 (v3.4.5)  
655 and stats (v4.2.2). Scripts are available in Github  
[https://github.com/hzuber67/Feature\\_analysisDNE1](https://github.com/hzuber67/Feature_analysisDNE1).

656

## 658 **Accession numbers**

659 Raw and processed sequences of RNAseq, SmallRNAseq, HyperTRIBEseq, and  
660 GMUCT libraries (Supplemental Data Set S1 to S4) are available at the National  
661 Center for Biotechnology Information (NCBI)- Sequence Read Archive (SRA) under  
662 the accession number PRJNA995202. Sequence corresponding to genes mentioned  
663 in this article can be found in the Arabidopsis Information Resource (TAIR \_  
664 <https://www.arabidopsis.org/>) under the following accession numbers: AT2G15560  
665 (DNE1); AT4G03210 (XTH9); AT3G13960 (GRF5); AT5G20700 (DUF581);  
666 AT4G29920 (SMXL4); AT1G54490 (XRN4); AT3G03300 (DCL2); AT5G20320  
667 (DCL4); AT5G13570 (DCP2); AT1G06150 (LHL1); AT2G31280 (LHL2/LL2);  
668 AT1G78080 (RAP2-4). CG12598 NM\_001297862 (ADAR isoform N).

669

## 670 Acknowledgements

671 The authors thank Peter Brodersen and Laura Arribas Hernandez for advices and for  
672 sending the plasmids containing the ADARcd domain used in HyperTRIBE and  
673 Sarah Rennie for support in using the HyperTRIBER pipeline. Sandrine Koehler  
674 from the Plateforme d'analyse d'expression génique for help in RNA-seq libraries  
675 preparation.

676

## 677 Author contribution

678 **Damien Garcia:** research design, conceptualization, data interpretation, initial  
679 analysis of HTS data, writing – original draft, writing – review and editing. **Aude**  
680 **Pouclet:** performed the experiments, collected and interpreted the data, writing –  
681 review and editing. **David Pfleiger:** analysis and visualization of HTS data, writing –  
682 review and editing. **Rémy Merret:** performed the GMUCT, writing – review and  
683 editing; **Marie-Christine Carpentier:** performed the primary analysis of GMUCT data,  
684 writing – review and editing. **Marlene Schiaffini** produced mutant combinations,  
685 writing – review and editing. **Hélène Zuber** performed statistical analysis and  
686 comparison of HTS datasets, writing – review and editing. **Dominique Gagliardi:**  
687 Conceptualization, data interpretation, writing – review and editing.

688

## 689 Funding

690 This work of the Interdisciplinary Thematic Institute IMCBio, as part of the ITI 2021-  
691 2028 program of the University of Strasbourg, CNRS and Inserm, was supported by  
692 IdEx Unistra (ANR-10-IDEX-0002), and by SFRI-STRAT'US project (ANR 20-SFRI-  
693 0012) and EUR IMCBio (ANR-17-EURE-0023) under the framework of the French  
694 Investments for the Future Program. Sequencing was performed by the GenomEast  
695 platform, a member of the “France Génomique” consortium (ANR-10-INBS-0009).  
696 Rémy Merret and Marie-Christine Carpentier work within the framework of the  
697 “Laboratoires d’Excellences (LABEX)” TULIP (ANR-10-LABX-41) and of the “École  
698 Universitaire de Recherche (EUR)” TULIP-GS (ANR-18-EURE-0019).

699

700

## 701 Figure legends

702

703 **Figure 1. *In vivo* editing using HyperTRIBE identifies mRNA in direct contact**

704 with DNE1. (A) Western blot showing the protein accumulation in transgenic lines

705 used for HyperTRIBE and expressing either the ADAR catalytic domain (ADAR) used

706 as a control or protein fusions between DNE1 and ADAR. (B) Venn diagram showing

707 the overlap in loci edited by ADAR-DNE1 or ADAR-DNE1<sup>D153N</sup>. Significant A to G

708 editions were considered with adjpv<0.01, Log2FC>1 and a minimum of 10 reads. (C)

709 Distribution of editions by DNE1 and DNE1<sup>D153N</sup> on mRNAs. (D) Schemes showing

710 the editions by ADAR-DNE1<sup>D153N</sup> on two transcripts (additional examples are shown

711 in Supplemental Fig. S1).

712

713 **Figure 2. Degradome analysis by GMUCT identifies two opposite trends on**

714 **DNE1 targets upon mutation in DNE1.** (A) Venn diagram showing the output of a

715 differential GMUCT analysis between *dne1 xrn4* and *xrn4* and displaying the overlap

716 between loci showing upregulated and downregulated 5'P fragments. (B) Plots

717 showing the repartition of downregulated 5'P on two loci presenting only

718 downregulated 5'P in *dne1 xrn4*. (C) Plots showing the repartition of 5'P on three loci

719 presenting both downregulated and upregulated 5'P in *dne1 xrn4*. Differential 5'P

720 were considered with Log2FC≥1 or Log2FC≤1 and Pv<0.05 following the DEXseq

721 analysis. Datasets from the three biological replicates were pooled to generate the

722 graphs presented in B and C. (D) Histogram showing the distribution on mRNAs of

723 5'P depending on their behavior in *dne1 xrn4*. (E) Analysis of the nucleotide

724 composition around the 1295 main DNE1 dependent 5'P site using a sequence logo.

725 The upper panel shows a control sequence logo produced using unchanged 5'P sites

726 in *dne1 xrn4* coming from the 1295 loci producing DNE1 dependent 5'P. The lower

727 panel shows the same analysis using the main DNE1 dependent 5'P from each locus.

728 Position 0 represents the first nucleotide of the 5'P as sequenced in GMUCT.

729

730 **Figure 3. Analysis of mRNA features enriched in mRNAs identified in**

731 **HyperTRIBE and GMUCT.**

732 (A) Venn diagram showing the overlap between loci edited by ADAR-DNE1<sup>D153N</sup> and

733 loci producing DNE1 dependent 5'P fragments. (B) Venn diagram showing the

734 overlap between loci edited by ADAR-DNE1<sup>D153N</sup> and transcripts containing validated

735 RNA-G quadruplex (rG4). (C) Boxplot analysis of the number of introns and of mRNA,

736 5' and 3' UTR lengths for the DNE-dependent loci identified by the different methods.

737 Significantly different values (adjpv < 0.001) are labelled by different letters (Wilcoxon

738 rank sum test). D) Proportion of transcripts containing uORFs or rG4 in the different

739 lists of DNE-dependent loci based on refs. Significantly different values (adjpv <

740 0.001) are labelled by different letters (two-samples z-test of proportions). In (C) and

741 (D) the lists of transcripts expressed in flowers and seedlings are used as control.

742

743 **Figure 4. Transcriptomic analysis of *dcp2*, *dne1 dcp2* and *xrn4* mutants identify**

744 **commonly deregulated transcripts.** (A) Plot showing the number of differentially

745 expressed genes in *dne1*, *dcp2*, *dne1 dcp2* and *xrn4* versus WT with adjPv<0.05

746 (n=3). (B) Venn diagram showing commonly upregulated loci between the two *dne1*

747 *dcp2* double mutants and *xrn4*. (C) Heatmap showing the mRNA accumulation  
748 pattern in *dne1*, *dcp2*, *dne1 dcp2* and *xrn4* for loci upregulated in both *dne1 dcp2*  
749 double mutants. (D) Venn diagram showing the overlap between upregulated loci in  
750 both *dne1 dcp2* double mutants and loci identified by GMUCT and HyperTRIBE.  
751

752 **Figure 5. Differential analysis of small RNA accumulation in *dcp2*, *dne1 dcp2* and *xrn4* mutants.** (A) Bar plots showing the output of the differential analysis of  
753 sRNA accumulation comparing mutants versus WT with adjPv<0.05 (n=3). (B) Venn  
754 diagram showing the overlap observed for upregulated sRNAs between different  
755 mutants. (C) Bar plots showing the output of the differential analysis of sRNA  
756 accumulation comparing *dne1 dcp2* versus *dcp2*. (D) Venn diagram showing the  
757 overlap observed for upregulated and downregulated sRNAs between the two *dne1*  
758 *dcp2* double mutants. (E) Northern blot showing sRNA accumulation for loci  
759 differentially accumulating in *dne1 dcp2* vs *dcp2*. The quantification is the mean and  
760 was performed with ImageJ on blots from three biological replicates. The 21nt size  
761 was determined by hybridization with an antisense probe targeting miR160. U6 was  
762 used as a loading control. (F) Plots showing the accumulation of mRNA-derived  
763 siRNAs along the transcripts for loci with upregulated and downregulated siRNAs.  
764 Datasets from the three biological replicates were pooled to generate these graphs.  
765 (G) Boxplot analysis of the number of introns and of mRNA, 5' and 3' UTR lengths for  
766 transcripts with differential sRNA accumulation in *xrn4*, *dcp2*, and *dne1 dcp2*.  
767 Significantly different values (adjpv < 0.001) are labelled by different letters (Wilcoxon  
768 rank sum test). (H) Proportion of transcripts containing uORFs or rG4 in the different  
769 lists of transcripts with differential sRNA accumulation. Significantly different values  
770 (adjpv < 0.001) are labelled by different letters (two-samples z-test of proportions). In  
771 (G) and (H) the list of transcripts expressed in flowers is used as control.  
772

773 **Figure 6. Diverse HTS techniques identifiy specific and common mRNAs influenced by DNE1.** Bubble chart showing the extent of intersection between the  
774 list of loci identified by sRNA-seq, HyperTRIBE and GMUCT. Each column  
775 corresponds to a list of loci and each row correspond to a possible intersection.  
776 Bubbles indicate the number of loci for each intersection with colors showing the  
777 number of related lists.  
778

779 **Figure 7. Models of DNE1 and DCP2 coordinated action on mRNAs.** (A), (B)  
780 Integrated models for the action of DNE1 and DCP2 on mRNA-derived siRNAs  
781 production. (C) Integrated model built from the HyperTRIBE and GMUCT data. The  
782 model shows interaction and action of DNE1 in the CDS on sites with preferred  
783 nucleotide composition. Enriched features in DNE1 targets including RNA-G4 and  
784 translated uORFs are depicted.  
785

786 **Supplemental data:**  
787  
788

790 **Supplemental Figure S1.** Schemes showing the editions by ADAR- DNE1<sup>D153N</sup> on  
791 11 transcripts illustrating the preferential edition in the CDS.

792  
793 **Supplemental Figure S2.** Profiles of 5'P fragments accumulation in GMUCT on  
794 representative examples. (A) Plots showing the repartition of 5'P on loci presenting  
795 only downregulated 5'P fragments. (B) Plots showing the repartition of 5'P on five loci  
796 presenting both downregulated and upregulated 5'P fragments. (C) Logo analysis  
797 performed on the 224 DNE1 targets identified in Nagarajan et al 2023.

798  
799 **Supplemental Figure S3.** Predicted expression patterns of AT2G31280 (LL2) and  
800 AT1G06150 (LHL1) in the shoot meristem of *Arabidopsis thaliana* using the 3D flower  
801 meristem tool from single cell experiments performed in Neumann et al 2022.

802  
803 **Supplemental Figure S4.** Representative examples of transcripts showing  
804 differential accumulation of mRNA-derived siRNAs between *dcp2* and *dne1 dcp2*. (A)  
805 Plots showing the accumulation of mRNA-derived siRNAs along the transcripts for  
806 upregulated siRNAs. (B) Plots showing the accumulation of mRNA-derived siRNAs  
807 along the transcripts for downregulated siRNAs.

808  
809 **Supplemental Table S1.** Primer list.

810  
811 **Supplemental Data Set S1.** HyperTRIBE data.

812  
813 **Supplemental Data Set S2.** GMUCT data.

814  
815 **Supplemental Data Set S3.** RNAseq data.

816  
817 **Supplemental Data Set S4.** sRNAseq data.

818  
819 **Supplemental Data Set S5.** Localization of differential sRNA on transcripts showing  
820 differential accumulation in *dne1 dcp2* vs *dcp2*.

821  
822 **Supplemental Data Set S6.** Statistics for feature enrichment analysis in Figure 3 and  
823 5.

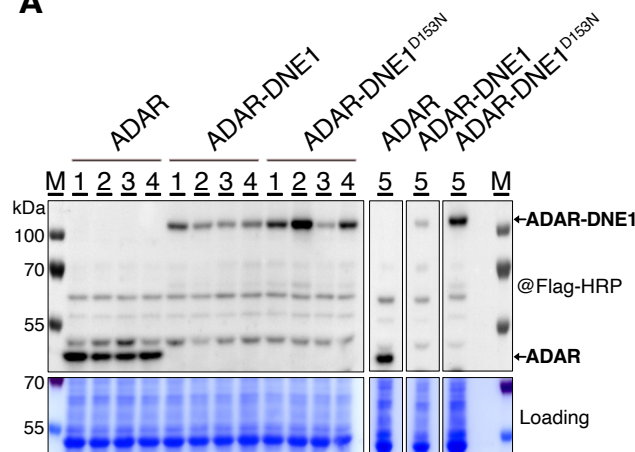
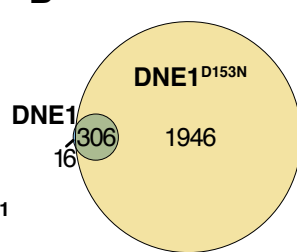
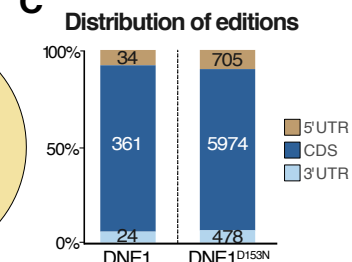
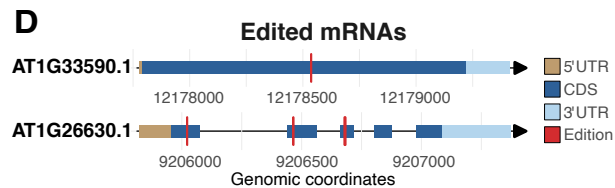
824  
825 **Supplemental Data Set S7.** Lists of loci used to identify mRNA features in Figure 3  
826 and 5.

827  
828  
829 **References**

830  
831 De Alba AEM, Moreno AB, Gabriel M, Mallory AC, Christ A, Bounon R, Balzergue S,  
832 Aubourg S, Gautheret D, Crespi MD, et al (2015) In plants, decapping prevents  
833 RDR6-dependent production of small interfering RNAs from endogenous mRNAs.

834 Nucleic Acids Res 43: 2902–2913  
835 Anders S, Reyes A, Huber W (2012) Detecting differential usage of exons from RNA-  
836 seq data. Genome Res 22: 2008  
837 Arribas-Hernández L, Rennie S, Köster T, Porcelli C, Lewinski M, Staiger D,  
838 Andersson R, Brodersen P (2021) Principles of mRNA targeting via the Arabidopsis  
839 m 6 A-binding protein ECT2. Elife. doi: 10.7554/ELIFE.72375  
840 Boehm V, Kueckelmann S, Gerbracht J V., Kallabis S, Britto-Borges T, Altmüller J,  
841 Krüger M, Dieterich C, Gehring NH (2021) SMG5-SMG7 authorize nonsense-  
842 mediated mRNA decay by enabling SMG6 endonucleolytic activity. Nat Commun. doi:  
843 10.1038/S41467-021-24046-3  
844 Branscheid A, Marchais A, Schott G, Lange H, Gagliardi D, Andersen SU, Voinnet O,  
845 Brodersen P (2015) SKI2 mediates degradation of RISC 5'-cleavage fragments and  
846 prevents secondary siRNA production from miRNA targets in Arabidopsis. Nucleic  
847 Acids Res 43: 10975–10988  
848 Bryksin A, Matsumura I (2013) Overlap extension PCR cloning. Methods Mol Biol  
849 1073: 31–42  
850 Carpentier MC, Bousquet-Antonelli C, Merret R (2021) Fast and Efficient 5'P  
851 Degradome Library Preparation for Analysis of Co-Translational Decay in  
852 Arabidopsis. Plants (Basel, Switzerland) 10: 1–10  
853 Chandler JW, Werr W (2020) A phylogenetically conserved APETALA2/ETHYLENE  
854 RESPONSE FACTOR, ERF12, regulates Arabidopsis floral development. Plant Mol  
855 Biol 102: 39–54  
856 Christie M, Croft LJ, Carroll BJ (2011) Intron splicing suppresses RNA silencing in  
857 Arabidopsis. Plant J 68: 159–167  
858 Clough SJ, Bent AF (1998) Floral dip: a simplified method for Agrobacterium-  
859 mediated transformation of *Arabidopsis thaliana*. Plant J 16: 735–743  
860 Ding D, Wei C, Dong K, Liu J, Stanton A, Xu C, Min J, Hu J, Chen C (2020) LOTUS  
861 domain is a novel class of G-rich and G-quadruplex RNA binding domain. Nucleic  
862 Acids Res 48: 9262–9272  
863 Gregory BD, O'Malley RC, Lister R, Urich MA, Tonti-Filippini J, Chen H, Millar AH,  
864 Ecker JR (2008) A link between RNA metabolism and silencing affecting Arabidopsis  
865 development. Dev Cell 14: 854–866  
866 He F, Jacobson A (2022) Eukaryotic mRNA decapping factors: molecular  
867 mechanisms and activity. FEBS J. doi: 10.1111/FEBS.16626  
868 Hu Q, Merchante C, Stepanova AN, Alonso JM, Heber S (2016) Genome-Wide  
869 Search for Translated Upstream Open Reading Frames in *Arabidopsis Thaliana*.  
870 IEEE Trans Nanobioscience 15: 150–159  
871 Krempl C, Lazzaretti D, Sprangers R (2023) A structural biology view on the enzymes  
872 involved in eukaryotic mRNA turnover. Biol Chem. doi: 10.1515/HSZ-2023-0182  
873 Lam P, Zhao L, Eveleigh N, Yu Y, Chen X, Kunst L (2015) The exosome and trans-  
874 acting small interfering RNAs regulate cuticular wax biosynthesis during *Arabidopsis*  
875 inflorescence stem development. Plant Physiol 167: 323–336  
876 Lange H, Gagliardi D (2022) Catalytic activities, molecular connections, and  
877 biological functions of plant RNA exosome complexes. Plant Cell 34: 967–988  
878 Lange H, Ndecky SYA, Gomez-Diaz C, Pflieger D, Butel N, Zumsteg J, Kuhn L,  
879 Piermaria C, Chicher J, Christie M, et al (2019) RST1 and RIPR connect the cytosolic  
880 RNA exosome to the Ski complex in *Arabidopsis*. Nat Commun. doi:  
881 10.1038/S41467-019-11807-4  
882 Lopez-Gomollon S, Baulcombe DC (2022) Roles of RNA silencing in viral and non-  
883 viral plant immunity and in the crosstalk between disease resistance systems. Nat

884 Rev Mol Cell Biol 23: 645–662  
885 Nagarajan VK, Kukulich PM, Von Hagel B, Green PJ (2019) RNA degradomes reveal  
886 substrates and importance for dark and nitrogen stress responses of *Arabidopsis*  
887 XRN4. *Nucleic Acids Res* 47: 9216–9230  
888 Nagarajan VK, Stuart CJ, DiBattista AT, Accerbi M, Caplan JL, Green PJ (2023) RNA  
889 degradome analysis reveals DNE1 endoribonuclease is required for the turnover of  
890 diverse mRNA substrates in *Arabidopsis*. *Plant Cell* 35: 1936–1955  
891 Nishimura T, Fakim H, Brandmann T, Youn JY, Gingras AC, Jinek M, Fabian MR  
892 (2018) Human MARF1 is an endoribonuclease that interacts with the DCP1:2  
893 decapping complex and degrades target mRNAs. *Nucleic Acids Res* 46: 12008–  
894 12021  
895 Poulsen C, Vaucheret H, Brodersen P (2013) Lessons on RNA silencing  
896 mechanisms in plants from eukaryotic argonaute structures. *Plant Cell* 25: 22–37  
897 Rahman R, Xu W, Jin H, Rosbash M (2018) Identification of RNA-binding protein  
898 targets with HyperTRIBE. *Nat Protoc* 13: 1829–1849  
899 Rehwinkel J, Behm-Ansmant I, Gatfield D, Izaurralde E (2005) A crucial role for  
900 GW182 and the DCP1:DCP2 decapping complex in miRNA-mediated gene silencing.  
901 *RNA* 11: 1640–1647  
902 Scheer H, de Almeida C, Ferrier E, Simonnot Q, Poirier L, Pflieger D, Sement FM,  
903 Koechler S, Piermaria C, Krawczyk P, et al (2021) The TUTase URT1 connects  
904 decapping activators and prevents the accumulation of excessively deadenylated  
905 mRNAs to avoid siRNA biogenesis. *Nat Commun.* doi: 10.1038/S41467-021-21382-2  
906 Schiaffini M, Chicois C, Pouclet A, Chartier T, Ubrig E, Gobert A, Zuber H, Mutterer J,  
907 Chicher J, Kuhn L, et al (2022) A NYN domain protein directly interacts with  
908 DECAPPING1 and is required for phyllotactic pattern. *Plant Physiol* 188: 1174–1188  
909 Schmid M, Jensen TH (2019) The Nuclear RNA Exosome and Its Cofactors. *Adv Exp  
910 Med Biol* 1203: 113–132  
911 Souret FF, Kastenmayer JP, Green PJ (2004) AtXRN4 degrades mRNA in  
912 *Arabidopsis* and its substrates include selected miRNA targets. *Mol Cell* 15: 173–183  
913 Vidya E, Duchaine TF (2022) Eukaryotic mRNA Decapping Activation. *Front Genet*  
914 13: 832547  
915 Willmann MR, Berkowitz ND, Gregory BD (2014) Improved genome-wide mapping of  
916 uncapped and cleaved transcripts in eukaryotes--GMUCT 2.0. *Methods* 67: 64–73  
917 Yang X, Cheema J, Zhang Y, Deng H, Duncan S, Umar MI, Zhao J, Liu Q, Cao X,  
918 Kwok CK, et al (2020) RNA G-quadruplex structures exist and function in vivo in  
919 plants. *Genome Biol.* doi: 10.1186/S13059-020-02142-9  
920 Zhang X, Zhu Y, Liu X, Hong X, Xu Y, Zhu P, Shen Y, Wu H, Ji Y, Wen X, et al (2015)  
921 Plant biology. Suppression of endogenous gene silencing by bidirectional  
922 cytoplasmic RNA decay in *Arabidopsis*. *Science* 348: 120–123  
923 Zhang Y, Mitsuda N, Yoshizumi T, Horii Y, Oshima Y, Ohme-Takagi M, Matsui M,  
924 Kakimoto T (2021) Two types of bHLH transcription factor determine the competence  
925 of the pericycle for lateral root initiation. *Nat plants* 7: 633–643  
926

**A****B****C****D**

**Figure 1. *In vivo* editing using HyperTRIBE identifies mRNA in direct contact with DNE1.** (A) Western blot showing the protein accumulation in transgenic lines used for HyperTRIBE and expressing either the ADAR catalytic domain (ADAR) used as a control or protein fusions between DNE1 and ADAR. (B) Venn diagram showing the overlap in loci edited by ADAR-DNE1 or ADAR-DNE1<sup>D153N</sup>. Significant A to G editions were considered with adjpv<0.01, Log2FC>1 and a minimum of 10 reads. (C) Distribution of editions by DNE1 and DNE1<sup>D153N</sup> on mRNAs. (D) Schemes showing the editions by ADAR-DNE1<sup>D153N</sup> on two transcripts (additional examples are shown in Supplemental Fig. S1).

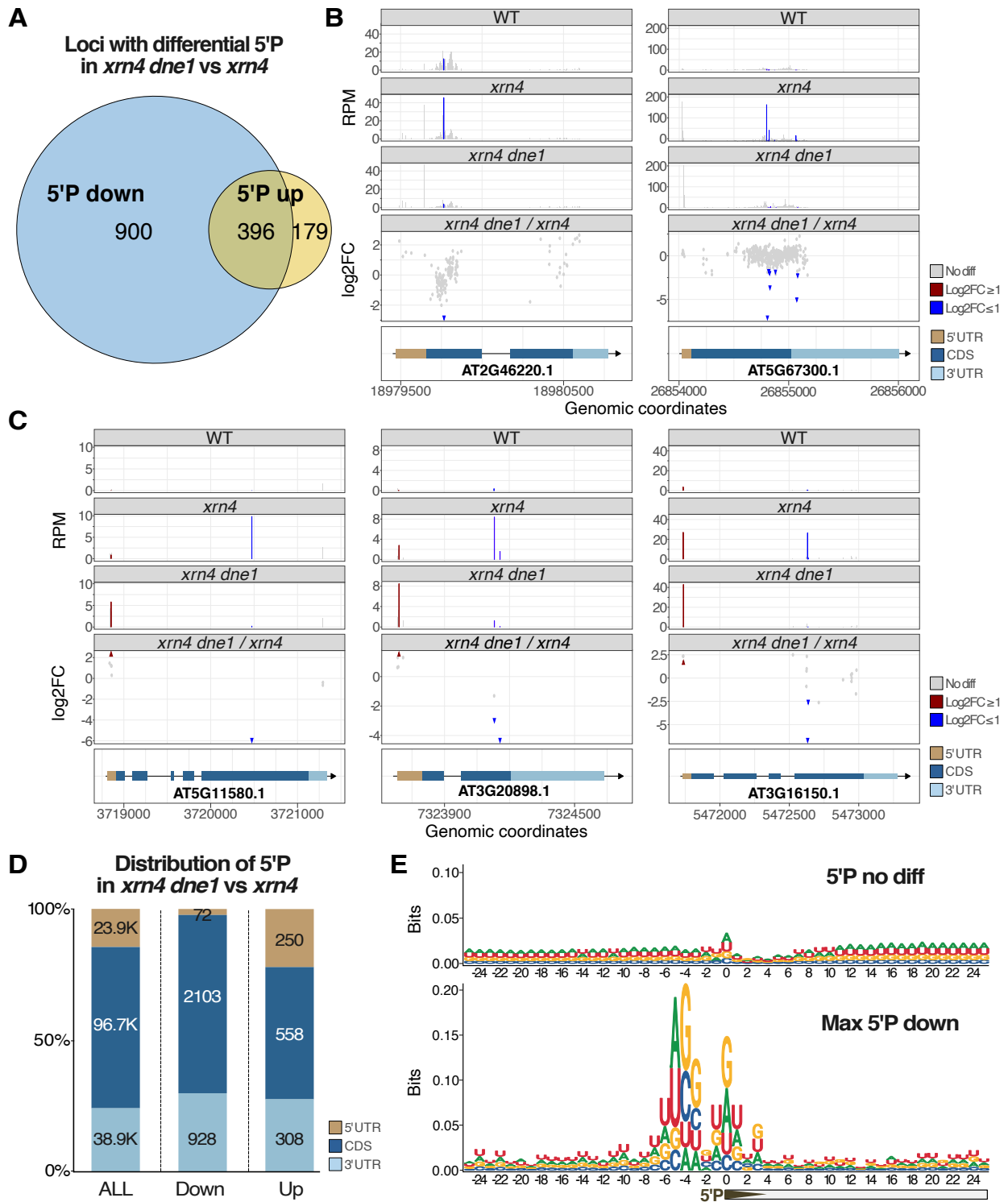


**Figure 2. Degradome analysis by GMUCT identifies two opposite trends on DNE1 targets upon mutation in DNE1.** (A) Venn diagram showing the output of a differential GMUCT analysis between *dne1 xrn4* and *xrn4* and displaying the overlap between loci showing upregulated and downregulated 5'P fragments. (B) Plots showing the repartition of downregulated 5'P on two loci presenting only downregulated 5'P in *dne1 xrn4*. (C) Plots showing the repartition of 5'P on three loci presenting both downregulated and upregulated 5'P in *dne1 xrn4*. Differential 5'P were considered with  $\text{Log2FC} \geq 1$  or  $\text{Log2FC} \leq 1$  and  $P_{\text{value}} < 0.05$  following the DEXseq analysis. Datasets from the three biological replicates were pooled to generate the graphs presented in B and C. (D) Histogram showing the distribution on mRNAs of 5'P depending on their behavior in *dne1 xrn4*. (E) Analysis of the nucleotide composition around the 1295 main DNE1 dependent 5'P site using a sequence logo. The upper panel shows a control sequence logo produced using unchanged 5'P sites in *dne1 xrn4* coming from the 1295 loci producing DNE1 dependent 5'P. The lower panel shows the same analysis using the main DNE1 dependent 5'P from each locus. Position 0 represents the first nucleotide of the 5'P as sequenced in GMUCT.

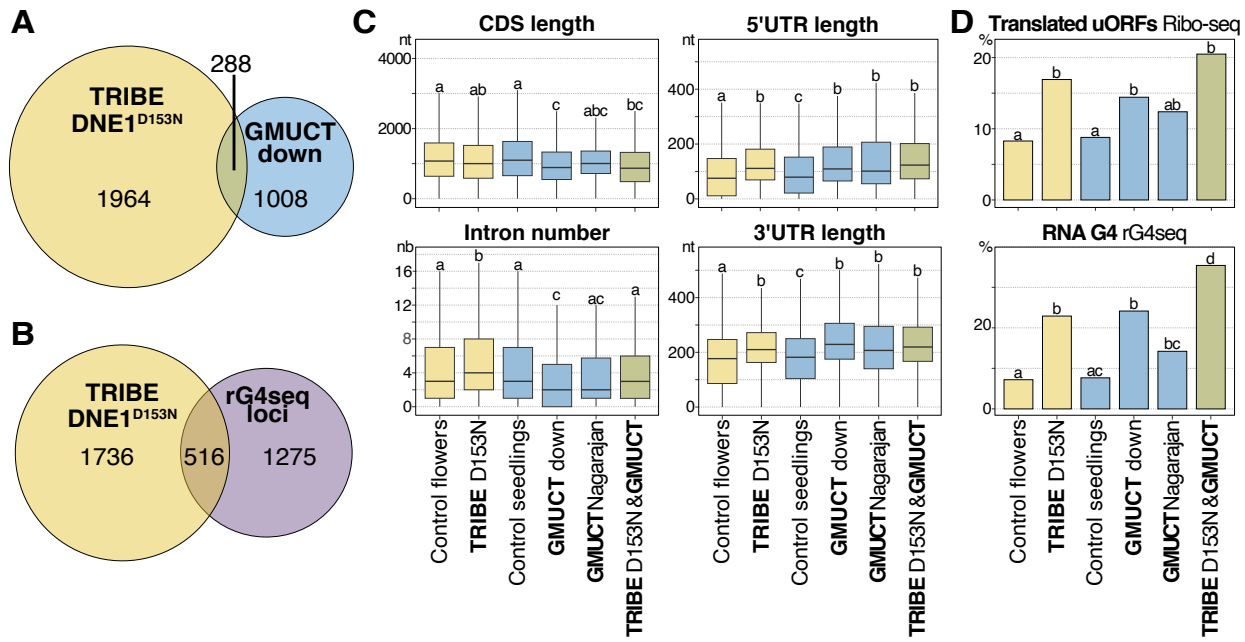


**Figure 3. Analysis of mRNA features enriched in mRNAs identified in HyperTRIBE and GMUCT.**

(A) Venn diagram showing the overlap between loci edited by ADAR-DNE1<sup>D153N</sup> and loci producing DNE1 dependent 5'P fragments. (B) Venn diagram showing the overlap between loci edited by ADAR-DNE1<sup>D153N</sup> and transcripts containing validated RNA-G quadruplex (rG4). (C) Boxplot analysis of the number of introns and of mRNA, 5' and 3' UTR lengths for the DNE-dependent loci identified by the different methods. Significantly different values (adjpv < 0.001) are labelled by different letters (Wilcoxon rank sum test). D) Proportion of transcripts containing uORFs or rG4 in the different lists of DNE-dependent loci based on refs. Significantly different values (adjpv < 0.001) are labelled by different letters (two-samples z-test of proportions). In (C) and (D) the lists of transcripts expressed in flowers and seedlings are used as control.

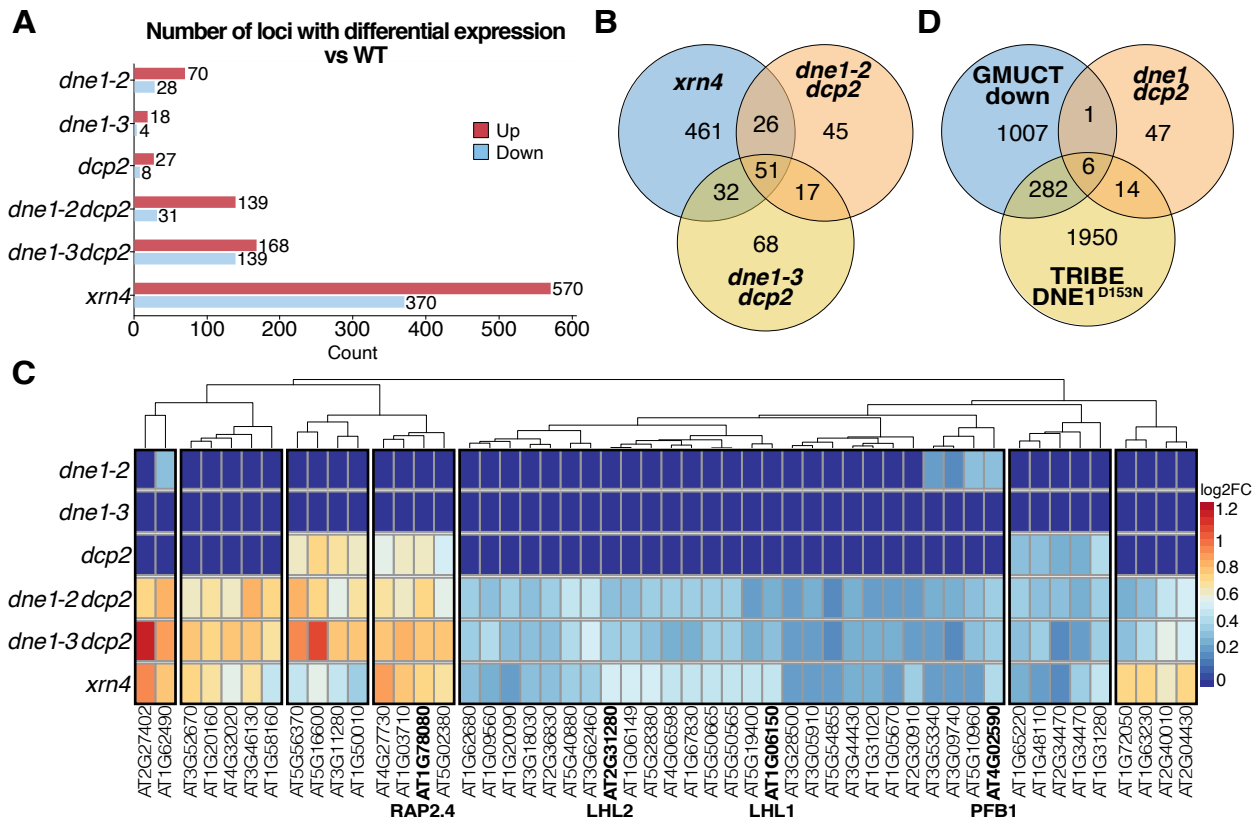


**Figure 4. Transcriptomic analysis of *dcp2*, *dne1 dcp2* and *xrn4* mutants identify commonly deregulated transcripts.** (A) Plot showing the number of differentially expressed genes in *dne1*, *dcp2*, *dne1 dcp2* and *xrn4* versus WT with adjPv<0.05 (n=3). (B) Venn diagram showing commonly upregulated loci between the two *dne1 dcp2* double mutants and *xrn4*. (C) Heatmap showing the mRNA accumulation pattern in *dne1*, *dcp2*, *dne1 dcp2* and *xrn4* for loci upregulated in both *dne1 dcp2* double mutants. (D) Venn diagram showing the overlap between upregulated loci in both *dne1 dcp2* double mutants and loci identified by GMUCT and HyperTRIBE.

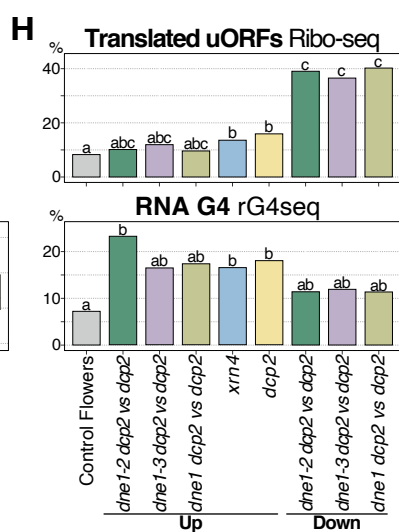
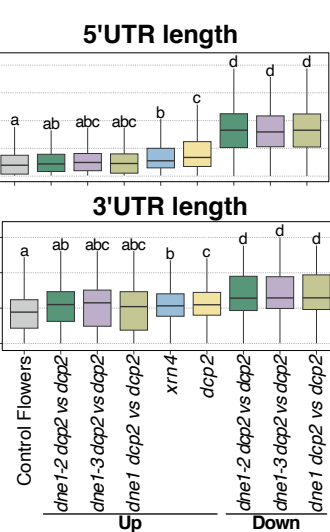
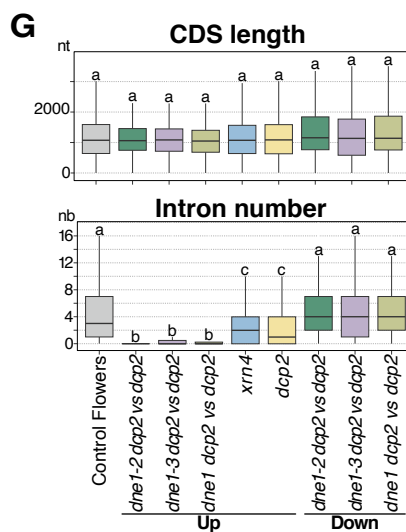
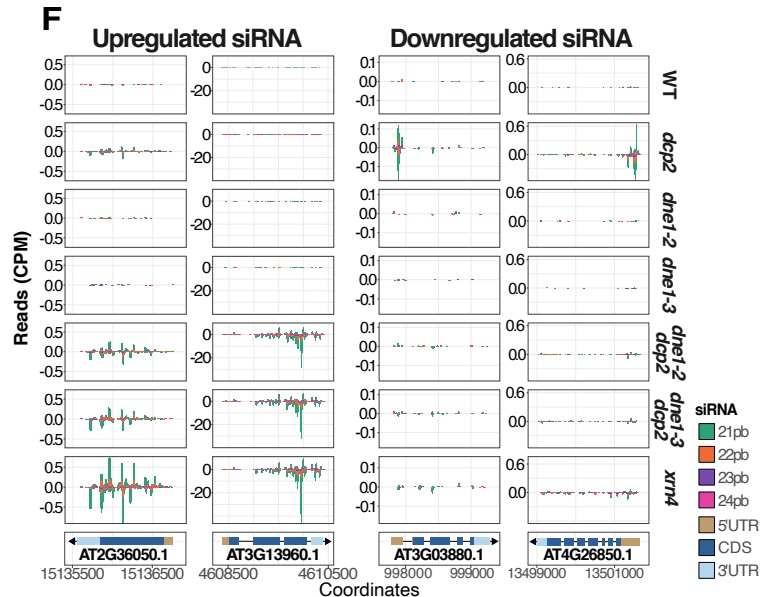
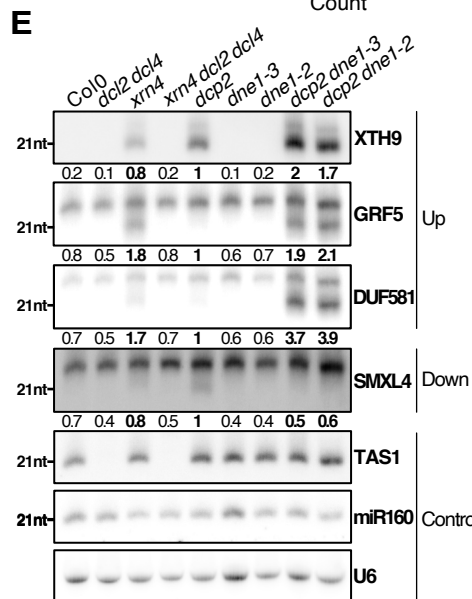
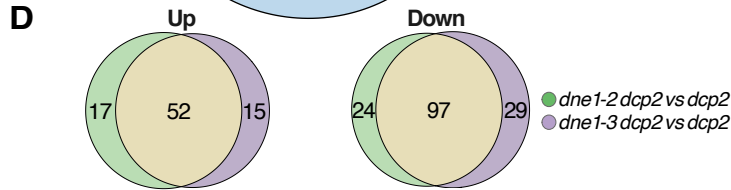
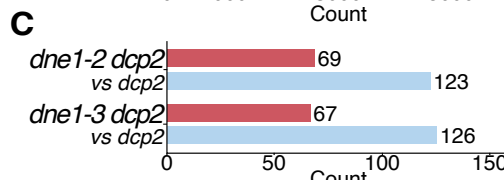
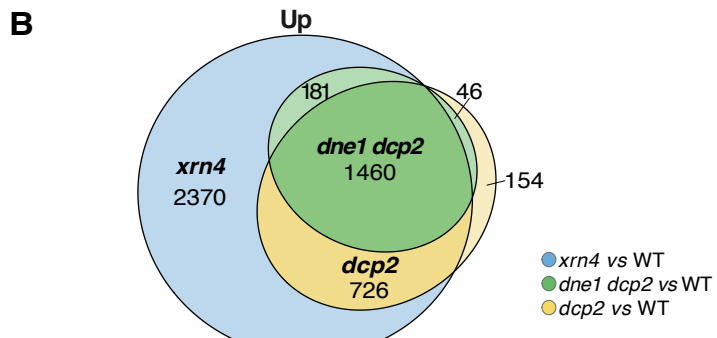
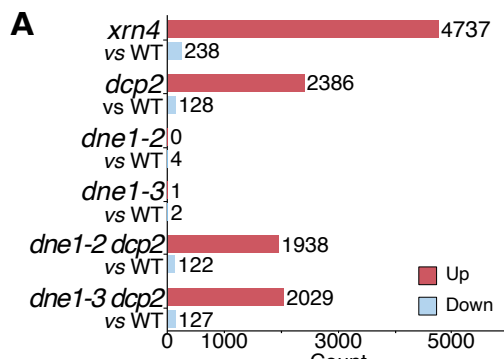


**Figure 5. Differential analysis of small RNA accumulation in *dcp2*, *dne1 dcp2* and *xrn4* mutants.** (A) Bar plots showing the output of the differential analysis of sRNA accumulation comparing mutants versus WT with adjPv<0.05 (n=3). (B) Venn diagram showing the overlap observed for upregulated sRNAs between different mutants. (C) Bar plots showing the output of the differential analysis of sRNA accumulation comparing *dne1 dcp2* versus *dcp2*. (D) Venn diagram showing the overlap observed for upregulated and downregulated sRNAs between the two *dne1 dcp2* double mutants. (E) Northern blot showing sRNA accumulation for loci differentially accumulating in *dne1 dcp2* vs *dcp2*. The quantification is the mean and was performed with ImageJ on blots from three biological replicates. The 21nt size was determined by hybridization with an antisense probe targeting miR160. U6 was used as a loading control. (F) Plots showing the accumulation of mRNA-derived siRNAs along the transcripts for loci with upregulated and downregulated siRNAs. Datasets from the three biological replicates were pooled to generate these graphs. (G) Boxplot analysis of the number of introns and of mRNA, 5' and 3' UTR lengths for transcripts with differential sRNA accumulation in *xrn4*, *dcp2*, and *dne1 dcp2*. Significantly different values (adjpv < 0.001) are labelled by different letters (Wilcoxon rank sum test). (H) Proportion of transcripts containing uORFs or rG4 in the different lists of transcripts with differential sRNA accumulation. Significantly different values (adjpv < 0.001) are labelled by different letters (two-samples z-test of proportions). In (G) and (H) the list of transcripts expressed in flowers is used as control.

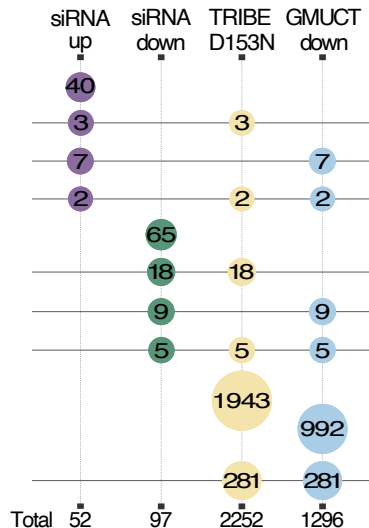


**Figure 6. Diverse HTS techniques identify specific and common mRNAs influenced by DNE1.** Bubble chart showing the extent of intersection between the list of loci identified by sRNA-seq, HyperTRIBE and GMUCT. Each column corresponds to a list of loci and each row correspond to a possible intersection. Bubbles indicate the number of loci for each intersection with colors showing the number of related lists.

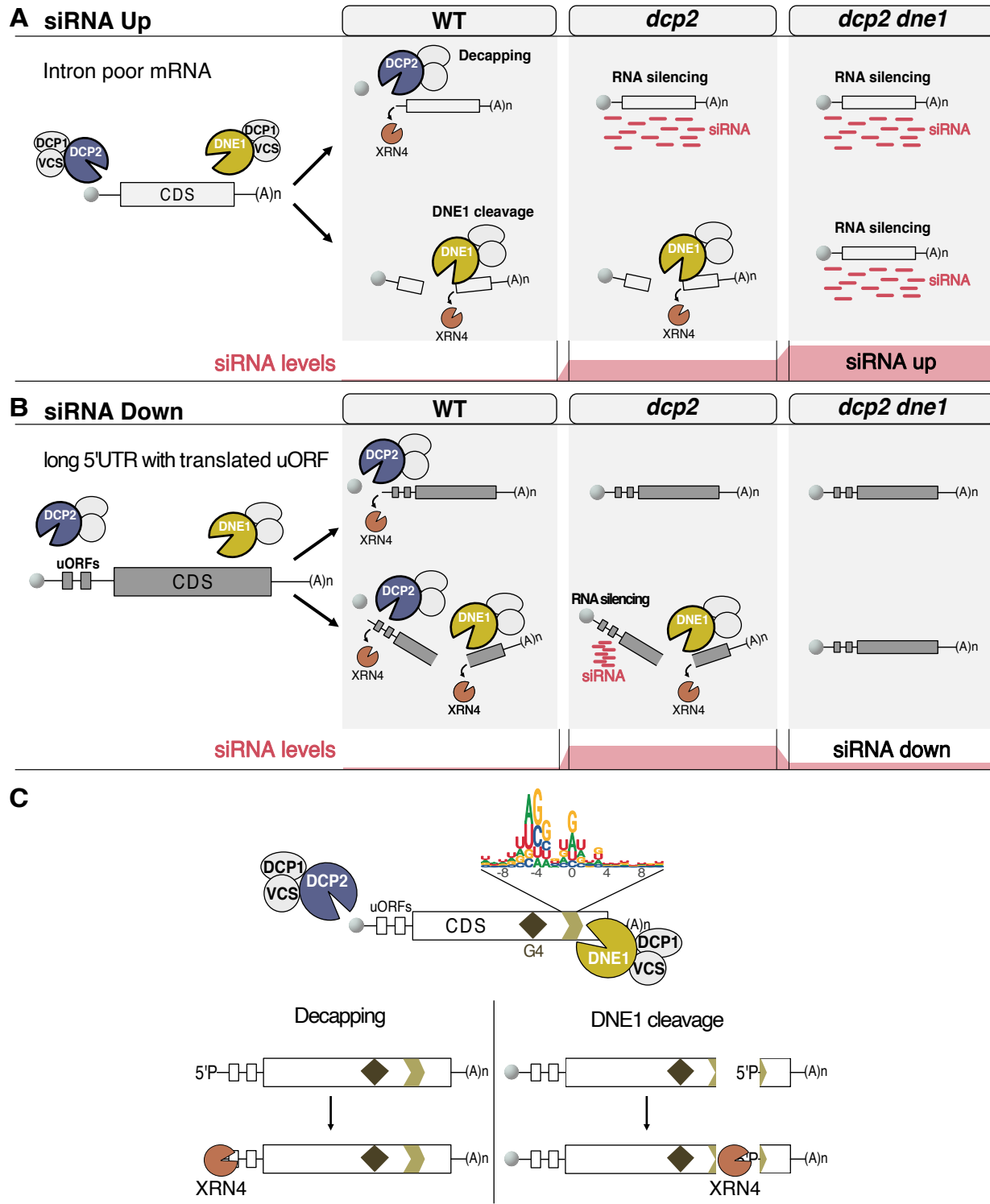


**Figure 7. Models of DNE1 and DCP2 coordinated action on mRNAs.** (A), (B) Integrated models for the action of DNE1 and DCP2 on mRNA-derived siRNAs production. (C) Integrated model built from the HyperTRIBE and GMUCT data. The model shows interaction and action of DNE1 in the CDS on sites with preferred nucleotide composition. Enriched features in DNE1 targets including RNA-G4 and translated uORFs are depicted.

## Parsed Citations

De Alba AEM, Moreno AB, Gabriel M, Mallory AC, Christ A, Bounon R, Balzergue S, Aubourg S, Gautheret D, Crespi MD, et al (2015) In plants, decapping prevents RDR6-dependent production of small interfering RNAs from endogenous mRNAs. *Nucleic Acids Res* 43: 2902–2913

Google Scholar: [Author Only](#) [Title Only](#) [Author and Title](#)

Anders S, Reyes A, Huber W (2012) Detecting differential usage of exons from RNA-seq data. *Genome Res* 22: 2008

Google Scholar: [Author Only](#) [Title Only](#) [Author and Title](#)

Arribas-Hernández L, Rennie S, Köster T, Porcelli C, Lewinski M, Staiger D, Andersson R, Brodersen P (2021) Principles of mRNA targeting via the *Arabidopsis* m6 A-binding protein ECT2. *Elife*. doi: 10.7554/ELIFE.72375

Google Scholar: [Author Only](#) [Title Only](#) [Author and Title](#)

Boehm V, Kueckelmann S, Gerbracht J V., Kallabis S, Britto-Borges T, Altmüller J, Krüger M, Dieterich C, Gehring NH (2021) SMG5-SMG7 authorize nonsense-mediated mRNA decay by enabling SMG6 endonucleolytic activity. *Nat Commun*. doi: 10.1038/S41467-021-24046-3

Google Scholar: [Author Only](#) [Title Only](#) [Author and Title](#)

Branscheid A, Marchais A, Schott G, Lange H, Gagliardi D, Andersen SU, Voinnet O, Brodersen P (2015) SKI2 mediates degradation of RISC 5'-cleavage fragments and prevents secondary siRNA production from miRNA targets in *Arabidopsis*. *Nucleic Acids Res* 43: 10975–10988

Google Scholar: [Author Only](#) [Title Only](#) [Author and Title](#)

Bryksin A, Matsumura I (2013) Overlap extension PCR cloning. *Methods Mol Biol* 1073: 31–42

Google Scholar: [Author Only](#) [Title Only](#) [Author and Title](#)

Carpentier MC, Bousquet-Antonacci C, Merret R (2021) Fast and Efficient 5'P Degradome Library Preparation for Analysis of Co-Translational Decay in *Arabidopsis*. *Plants* (Basel, Switzerland) 10: 1–10

Google Scholar: [Author Only](#) [Title Only](#) [Author and Title](#)

Chandler JW, Werr W (2020) A phylogenetically conserved APETALA2/ETHYLENE RESPONSE FACTOR, ERF12, regulates *Arabidopsis* floral development. *Plant Mol Biol* 102: 39–54

Google Scholar: [Author Only](#) [Title Only](#) [Author and Title](#)

Christie M, Croft LJ, Carroll BJ (2011) Intron splicing suppresses RNA silencing in *Arabidopsis*. *Plant J* 68: 159–167

Google Scholar: [Author Only](#) [Title Only](#) [Author and Title](#)

Clough SJ, Bent AF (1998) Floral dip: a simplified method for *Agrobacterium*-mediated transformation of *Arabidopsis thaliana*. *Plant J* 16: 735–743

Google Scholar: [Author Only](#) [Title Only](#) [Author and Title](#)

Ding D, Wei C, Dong K, Liu J, Stanton A, Xu C, Min J, Hu J, Chen C (2020) LOTUS domain is a novel class of G-rich and G-quadruplex RNA binding domain. *Nucleic Acids Res* 48: 9262–9272

Google Scholar: [Author Only](#) [Title Only](#) [Author and Title](#)

Gregory BD, O'Malley RC, Lister R, Urich MA, Tonti-Filippini J, Chen H, Millar AH, Ecker JR (2008) A link between RNA metabolism and silencing affecting *Arabidopsis* development. *Dev Cell* 14: 854–866

Google Scholar: [Author Only](#) [Title Only](#) [Author and Title](#)

He F, Jacobson A (2022) Eukaryotic mRNA decapping factors: molecular mechanisms and activity. *FEBS J*. doi: 10.1111/FEBS.16626

Google Scholar: [Author Only](#) [Title Only](#) [Author and Title](#)

Hu Q, Merchante C, Stepanova AN, Alonso JM, Heber S (2016) Genome-Wide Search for Translated Upstream Open Reading Frames in *Arabidopsis Thaliana*. *IEEE Trans Nanobioscience* 15: 150–159

Google Scholar: [Author Only](#) [Title Only](#) [Author and Title](#)

Krempl C, Lazzaretti D, Sprangers R (2023) A structural biology view on the enzymes involved in eukaryotic mRNA turnover. *Biol Chem*. doi: 10.1515/HSZ-2023-0182

Google Scholar: [Author Only](#) [Title Only](#) [Author and Title](#)

Lam P, Zhao L, Eveleigh N, Yu Y, Chen X, Kunst L (2015) The exosome and trans-acting small interfering RNAs regulate cuticular wax biosynthesis during *Arabidopsis* inflorescence stem development. *Plant Physiol* 167: 323–336

Google Scholar: [Author Only](#) [Title Only](#) [Author and Title](#)

Lange H, Gagliardi D (2022) Catalytic activities, molecular connections, and biological functions of plant RNA exosome complexes. *Plant Cell* 34: 967–988

Google Scholar: [Author Only](#) [Title Only](#) [Author and Title](#)

Lange H, Ndecky SYA, Gomez-Diaz C, Pflieger D, Butel N, Zumsteg J, Kuhn L, Piermaria C, Chicher J, Christie M, et al (2019) RST1 and RIPR connect the cytosolic RNAexosome to the Ski complex in *Arabidopsis*. *Nat Commun.* doi: 10.1038/S41467-019-11807-4

Google Scholar: [Author Only](#) [Title Only](#) [Author and Title](#)

Lopez-Gomollon S, Baulcombe DC (2022) Roles of RNA silencing in viral and non-viral plant immunity and in the crosstalk between disease resistance systems. *Nat Rev Mol Cell Biol* 23: 645–662

Google Scholar: [Author Only](#) [Title Only](#) [Author and Title](#)

Nagarajan VK, Kukulich PM, Von Hagel B, Green PJ (2019) RNA degradomes reveal substrates and importance for dark and nitrogen stress responses of *Arabidopsis* XRN4. *Nucleic Acids Res* 47: 9216–9230

Google Scholar: [Author Only](#) [Title Only](#) [Author and Title](#)

Nagarajan VK, Stuart CJ, DiBattista AT, Accerbi M, Caplan JL, Green PJ (2023) RNA degradome analysis reveals DNE1 endoribonuclease is required for the turnover of diverse mRNA substrates in *Arabidopsis*. *Plant Cell* 35: 1936–1955

Google Scholar: [Author Only](#) [Title Only](#) [Author and Title](#)

Nishimura T, Fakim H, Brandmann T, Youn JY, Gingras AC, Jinek M, Fabian MR (2018) Human MARF1 is an endoribonuclease that interacts with the DCP1:2 decapping complex and degrades target mRNAs. *Nucleic Acids Res* 46: 12008–12021

Google Scholar: [Author Only](#) [Title Only](#) [Author and Title](#)

Poulsen C, Vaucheret H, Brodersen P (2013) Lessons on RNA silencing mechanisms in plants from eukaryotic argonaute structures. *Plant Cell* 25: 22–37

Google Scholar: [Author Only](#) [Title Only](#) [Author and Title](#)

Rahman R, Xu W, Jin H, Rosbash M (2018) Identification of RNA-binding protein targets with HyperTRIBE. *Nat Protoc* 13: 1829–1849

Google Scholar: [Author Only](#) [Title Only](#) [Author and Title](#)

Rehwinkel J, Behm-Ansmant I, Gatfield D, Izaurralde E (2005) A crucial role for GW182 and the DCP1:DCP2 decapping complex in miRNA-mediated gene silencing. *RNA* 11: 1640–1647

Google Scholar: [Author Only](#) [Title Only](#) [Author and Title](#)

Scheer H, de Almeida C, Ferrier E, Simonnot Q, Poirier L, Pflieger D, Sement FM, Koechler S, Piermaria C, Krawczyk P, et al (2021) The TUTase URT1 connects decapping activators and prevents the accumulation of excessively deadenylated mRNAs to avoid siRNA biogenesis. *Nat Commun.* doi: 10.1038/S41467-021-21382-2

Google Scholar: [Author Only](#) [Title Only](#) [Author and Title](#)

Schiaffini M, Chicois C, Pouclet A, Chartier T, Ubrig E, Gobert A, Zuber H, Mutterer J, Chicher J, Kuhn L, et al (2022) ANYN domain protein directly interacts with DECAPPING1 and is required for phyllotactic pattern. *Plant Physiol* 188: 1174–1188

Google Scholar: [Author Only](#) [Title Only](#) [Author and Title](#)

Schmid M, Jensen TH (2019) The Nuclear RNA Exosome and Its Cofactors. *Adv Exp Med Biol* 1203: 113–132

Google Scholar: [Author Only](#) [Title Only](#) [Author and Title](#)

Souret FF, Kastenmayer JP, Green PJ (2004) AtXRN4 degrades mRNA in *Arabidopsis* and its substrates include selected miRNA targets. *Mol Cell* 15: 173–183

Google Scholar: [Author Only](#) [Title Only](#) [Author and Title](#)

Vidya E, Duchaine TF (2022) Eukaryotic mRNA Decapping Activation. *Front Genet* 13: 832547

Google Scholar: [Author Only](#) [Title Only](#) [Author and Title](#)

Willmann MR, Berkowitz ND, Gregory BD (2014) Improved genome-wide mapping of uncapped and cleaved transcripts in eukaryotes--GMICT 2.0. *Methods* 67: 64–73

Google Scholar: [Author Only](#) [Title Only](#) [Author and Title](#)

Yang X, Cheema J, Zhang Y, Deng H, Duncan S, Umar MI, Zhao J, Liu Q, Cao X, Kwok CK, et al (2020) RNA G-quadruplex structures exist and function in vivo in plants. *Genome Biol.* doi: 10.1186/S13059-020-02142-9

Google Scholar: [Author Only](#) [Title Only](#) [Author and Title](#)

Zhang X, Zhu Y, Liu X, Hong X, Xu Y, Zhu P, Shen Y, Wu H, Ji Y, Wen X, et al (2015) Plant biology. Suppression of endogenous gene silencing by bidirectional cytoplasmic RNA decay in *Arabidopsis*. *Science* 348: 120–123

Google Scholar: [Author Only](#) [Title Only](#) [Author and Title](#)

Zhang Y, Mitsuda N, Yoshizumi T, Horii Y, Oshima Y, Ohme-Takagi M, Matsui M, Kakimoto T (2021) Two types of bHLH transcription factor determine the competence of the pericycle for lateral root initiation. *Nat plants* 7: 633–643

Google Scholar: [Author Only](#) [Title Only](#) [Author and Title](#)